Available online at www.sciencedirect.com
ScienceDirect
Comput. Methods Appl. Mech. Engrg. 373 (2021) 113502
Computer methods in applied mechanics and engineering
www.elsevier.com/locate/cma

A novel fully-decoupled, second-order and energy stable numerical scheme of the conserved Allen–Cahn type flow-coupled binary surfactant model

Xiaofeng Yang

Department of Mathematics, University of South Carolina, Columbia, SC 29208, United States of America

Received 6 June 2020; received in revised form 7 October 2020; accepted 11 October 2020
Available online 16 November 2020

Abstract

In this paper, we establish a binary fluid surfactant model by coupling two mass-conserved Allen–Cahn equations and the Navier–Stokes equations and consider numerical simulations of the developed model. Due to a large number of nonlinear and nonlocal coupling terms in the model, it is very challenging to design an efficient and accurate numerical scheme, especially the full decoupling scheme with second-order time accuracy. We solve this challenge by developing a novel fully-decoupled approach, where the key idea achieving the full decoupling structure is to introduce an ordinary differential equation to deal with the nonlinear coupling terms that satisfy the so-called "*zero-energy-contribution*" property. In this way, we can easily discretize the coupled nonlinear terms in a fully explicit way, while still maintaining unconditional energy stability. By combining with the projection type method and quadratization approach, at each time step, we only need to solve several fully-decoupled linear elliptic equations with constant coefficients. We strictly prove the solvability of the scheme, prove that the scheme satisfies the unconditional energy stability, and give various 2D and 3D numerical simulations to show its stability and accuracy numerically. *As far as the author knows, this is the first fully-decoupled and second-order time-accurate scheme of the flow-coupled phase-field type model.*

Keywords: Fully-decoupled; Second-order; Phase-field; Fluid-surfactant; Conserved Allen–Cahn; Unconditional energy stability

1. Introduction

The earliest modeling work on binary fluid surfactants using the phase-field method can be traced back to the pioneering work of Laradji et al. [1,2], in which two phase-field variables are used to describe the local density of the fluid and the local concentration of the surfactant, respectively. Since the volume (or mass) of the two fluid components does not change with time, the Cahn–Hilliard dynamics (or H^{-1} gradient flow method), due to its conservation property, is usually used to derive the entire system containing two highly coupled nonlinear Cahn–Hilliard equations. The free energy of the system needs to be able to describe the hydrophilic–hydrophobic interaction of the fluid and the interfacial absorption characteristics caused by the amphiphilic molecules of the surfactant. Then, the system is derived by using the energetic variational approach. Moreover, if it is expected that the model can simulate the dynamics related to fluid flow, such as droplets coalescence/non-merging phenomena

E-mail address: xfyang@math.sc.edu.

https://doi.org/10.1016/j.cma.2020.113502
0045-7825/

under the shear flow [3,4], then the Navier–Stokes equations need to be combined with the phase-field system through the surface tension and advection derived using the Fick's law. For modeling/analysis/simulation work on the phase-field surfactant system, we refer to [5–11].

In this paper, we consider the numerical approximations of the hydrodynamics coupled binary surfactant model. Unlike the traditional way of using the Cahn–Hilliard dynamics (usually fourth-order system) to derive the model, we use the second-order Allen–Cahn dynamics (or L^2 gradient flow method) to establish a new model. This is because the Allen–Cahn system is relatively easier to solve numerically since it is usually second-order less than the Cahn–Hilliard system. We know that the inherent bottleneck of using the Allen–Cahn model is that it cannot conserve the volume over time. To solve this problem, we modify the model by adding a nonlocal Lagrangian multiplier to each phase-field equation. This term helps to maintain the law of energy and accurately retain the volume conservation. For the new model, we aim to develop effective numerical schemes that can have the fully-decoupled feature, unconditional energy stability, and second-order accuracy.

It is worth noting that although there exist many effective numerical schemes to simulate the phase-field binary fluid surfactant model, see [3,12–14], however, as far as the author knows, for the full flow coupling system, there is currently no successful method that can achieve the second-order accuracy in time and completely independent calculation of all variables (that is, a fully-decoupled scheme). The main difficulty is that the velocity field and phase-field variables are tightly coupled by the nonlinear surface tension and advection terms, and we lack efficient numerical tools to decouple them while preserving the unconditional energy stability. Therefore, even though both the fluid equations and the Cahn–Hilliard equations have many effective schemes, for example, the projection method [15–22], the linear stabilization [23–25], convex splitting [26–30], quadratization (IEQ [31–34] and SAV [35–37]), nonlinear derivative [38], nonlinear quadrature [39–41] methods, etc., after coupling these two types of equations, the processing of coupling terms by conventional simple explicit or implicit methods will inevitably lead to fully coupled or energy unstable schemes. To the best of the author's knowledge, the only fully-decoupled scheme that can achieve unconditional energy stability is developed in [42] which is obtained by adding a stabilization term to the advective velocity. However, the scheme is only first-order accurate in time and it is very difficult to generalize a similar idea to the second-order version to achieve the full decoupling and unconditional energy stability. Moreover, although the scheme given in [42] is fully-decoupled, its computational cost is high because it needs to solve the phase-field equation with variable coefficients at each time step.

Therefore, for the new Allen–Cahn type conserved flow-coupled binary surfactant model, this paper attempts to construct a novel method to achieve the characteristics of linearity, full decoupling, unconditional energy stability, and second-order accuracy in time. To this goal, when developing numerical algorithms, we turn our attention to using the well-known but often overlooked *"zero-energy-contribution"* property satisfied by the advection and surface tension terms. That is, when deducing the energy law, after applying the inner products of some appropriate functions, the resulting terms generated by these two terms will completely cancel out. Thus, using this property, we introduce a nonlocal variable and design an ordinary differential equation (ODE) associated with it, which contains the inner products of the advections and surface tensions with some specific functions. This ODE is trivial at the continuous level because all the terms in it are zero. But after discretization, it can help eliminate all the troublesome nonlinear terms to obtain unconditional energy stability. Meanwhile, the introduction of the nonlocal variable can decompose each discrete equation into multiple sub-equations that can be solved independently, thereby obtaining a fully-decoupled structure.

By combining this novel method with the existing proven effective methods (including the projection method for the Navier–Stokes equations, and the SAV method that linearizes the nonlinear energy potential), we obtain the desired scheme which is unconditionally energy stable, linear, fully-decoupled, second-order time-accurate. It should be emphasized that this technique of achieving the fully-decoupled scheme can be used in many complex coupled models as long as the coupling terms satisfy the so-called "zero-energy-contribution" characteristic. In other words, if the nonlinear coupling terms contained in the model do not have any contribution to the total free energy after taking the inner products with certain test functions when deriving the PDE energy law, this method is always applicable. The implementation of the scheme is very simple. At each time step, one only needs to solve a few fully-decoupled linear elliptic equations with constant coefficients. We strictly prove the unconditional energy stability of the scheme and then give many 2D and 3D numerical simulations to prove its stability and accuracy numerically.

The rest of the paper is organized as follows. In Section 2, we establish the conserved Allen–Cahn type hydrodynamics coupled binary fluid surfactant model and derive its energy structure. In Section 3, we construct

a second-order fully-decoupled numerical scheme and describe its implementations in detail. The unconditional energy stability is proved rigorously as well. In Section 4, numerous accuracy/stability tests and simulations in 2D and 3D are performed to demonstrate the effectiveness of the developed model and scheme. Some concluding remarks are presented in Section 5.

2. Governing system

We now develop the volume-conserved, hydrodynamically coupled Allen–Cahn type phase-field model for the binary surfactant system. Suppose $\Omega \in \mathbb{R}^d$ with $d = 2, 3$ is a smooth, open, bounded, connected domain, two local variables $\phi(\boldsymbol{x}, t)$ and $\rho(\boldsymbol{x}, t)$ are used to simulate the dynamics in a binary fluid-surfactant system, where ϕ is defined to represent the density (or volume fraction) of the two fluids, e.g., water and oil, i.e.,

$$\phi(\boldsymbol{x}, t) = \begin{cases} 1 & \text{fluid I}, \\ -1 & \text{fluid II}, \end{cases} \tag{2.1}$$

with a thin, smooth transition region with a width $O(\epsilon)$; and ρ is introduced to represent the local concentration of surfactants. The interface of the fluid mixture is described by the zero level set given by $\Gamma_t = \{\boldsymbol{x} : \phi(\boldsymbol{x}, t) = 0\}$. Hence, we consider the total free energy as follows [3,4,7,8],

$$E(\phi, \rho, \mathbf{u}) = \int_\Omega \Big\{ \frac{1}{2}|\mathbf{u}|^2 + \lambda_1 (\frac{1}{2}|\nabla\phi|^2 + \frac{1}{\epsilon^2} F(\phi)) + \lambda_2 (\frac{\gamma}{2}|\nabla\rho|^2 + \frac{1}{\eta^2} G(\rho)) + W(\phi, \rho) \Big\} d\boldsymbol{x} \tag{2.2}$$

where $\mathbf{u}$ is the average velocity field,

$$\begin{cases} F(\phi) = \dfrac{1}{4}(\phi^2 - 1)^2, \;\; W(\phi, \rho) = -\dfrac{\theta_1}{2}\rho|\nabla\phi|^2 + \dfrac{\theta_2}{2}\rho\phi^2 + \dfrac{\zeta}{4}|\nabla\phi|^4, \\ G(\rho) = \alpha_4\rho^4 + \alpha_3\rho^3 + \alpha_2\rho^2 + \alpha\rho, \; (\alpha_1, \alpha_2, \alpha_3, \alpha_4) = (3.62, -7.25, 7.30, -3.68), \end{cases} \tag{2.3}$$

and $\lambda_1, \lambda_2, \epsilon, \gamma, \eta, \theta_1, \theta_2, \zeta$ are all positive parameters. We note that the total free energy includes four parts. The first part is the kinetic energy. The second part includes the hydrophilic (gradient)-hydrophobic (double-well) tendency of the phase-field variable ϕ where the parameter ϵ represents the width of the binary fluid interface. The third part is the hydrophilicity (gradient)-hydrophobic (quartic polynomial G) tendency of the concentration variable ρ where η is the penalty parameter. The fourth part is the coupling item between the surfactant and the fluid interface, where the θ_1 term controls the degree of the effect of the surfactant on the fluid interface, θ_2 term guarantees a low concentration of surfactant in the bulk phase, and the ζ term ($\zeta \ll 1$) is used to ensure that the total free energy is bounded from below, see [4].

Remark 2.1. Note in many works, the hydrophobic potential for ρ is set to be the Flory–Huggins logarithmic type that reads as $\tilde{G}(\rho) = \rho\ln\rho + (1-\rho)\ln(1-\rho)$, see [4,7,8]. In this paper, we use a new quartic function $G(\rho)$ to replace it and $G(\rho)$ is obtained from the following relationship $G(0) = 0, G(\frac{1}{4}) = \tilde{G}(\frac{1}{4}), G(\frac{1}{2}) = \tilde{G}(\frac{1}{2}), G(\frac{3}{4}) = \tilde{G}(\frac{3}{4}), G(1) = 0$. The reasons for using this simple quartic polynomial include, (i) from Fig. 2.1, we can see that $G(\rho)$ and $\tilde{G}(\rho)$ are very consistent; (ii) the domain of logarithmic potential is an open interval $(0, 1)$, so it must be strictly ensured that the calculated value is in this range, otherwise, the calculation is easy to overflow, but this requirement is quite difficult to realize; (iii) the main purpose of this article is to give a simple and easy to calculate binary surfactant model, just like we use the second-order Allen–Cahn model to replace Cahn–Hilliard dynamics, a relatively simple fourth-order polynomial potential $G(\rho)$ is more preferred from the same reason; and (iv) the numerical results obtained using the two models are compared in Section 4 and the equilibrium solutions are essentially the same.

Then, by using the Allen–Cahn type (L^2-gradient flow) relaxation kinetics for ϕ and ρ, and assuming that the fluid is incompressible and follows the generalized Fick's law, that is, the mass flux is proportional to the gradient of the chemical potential, we get the hydrodynamics coupled binary surfactant model which reads as:

$$\phi_t + \nabla\cdot(\mathbf{u}\phi) = -M_1 \left(\mu - \frac{1}{|\Omega|}\int_\Omega \mu d\boldsymbol{x} \right), \tag{2.4}$$

$$\mu = \frac{\delta E}{\delta \phi} = \lambda_1(-\Delta\phi + \frac{1}{\epsilon^2} f(\phi)) + W_\phi, \tag{2.5}$$

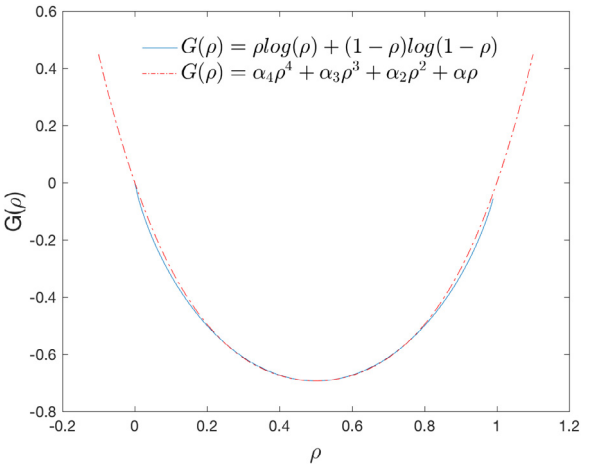

Fig. 2.1. The comparisons of the potential $G(\phi)$ using the quartic polynomial form and the Flory–Huggins logarithmic form.

$$\rho_t + \nabla\cdot(\mathbf{u}\rho) = -M_2\left(\omega - \frac{1}{|\Omega|}\int_\Omega \omega d\boldsymbol{x}\right), \tag{2.6}$$

$$\omega = \frac{\delta E}{\delta\rho} = \lambda_2(-\gamma\Delta\rho + \frac{1}{\eta^2}g(\rho)) + W_\rho, \tag{2.7}$$

$$\mathbf{u}_t + (\mathbf{u}\cdot\nabla)\mathbf{u} + \nabla p - \nu\Delta\mathbf{u} + \phi\nabla\mu + \rho\nabla\omega = 0, \tag{2.8}$$

$$\nabla\cdot\mathbf{u} = 0, \tag{2.9}$$

where

$$\begin{cases} W_\phi = \dfrac{\delta W(\phi,\rho)}{\delta\phi} = \theta_1\nabla\cdot(\rho\nabla\phi) + \theta_2\rho\phi - \zeta\nabla\cdot(|\nabla\phi|^2\nabla\phi), \\ W_\rho = \dfrac{\delta W(\phi,\rho)}{\delta\rho} = -\dfrac{\theta_1}{2}|\nabla\phi|^2 + \dfrac{\theta_2}{2}\phi^2,\ f(\phi) = F'(\phi) = \phi(\phi^2-1),\ g(\rho) = G'(\rho), \end{cases} \tag{2.10}$$

where M_1, M_2 are two mobility parameters, ν is the fluid viscosity, p is the pressure, and two nonlinear terms $\phi\nabla\mu$ and $\rho\nabla\omega$ are surface tensions.

In this paper, we consider the following two kinds of boundary conditions:

$$(i)\ \text{all variables are periodic; or} \tag{2.11}$$

$$(ii)\ \mathbf{u}|_{\partial\Omega} = \mathbf{0},\ \partial_{\boldsymbol{n}}\phi|_{\partial\Omega} = \partial_{\boldsymbol{n}}\rho|_{\partial\Omega} = 0, \tag{2.12}$$

where $\boldsymbol{n}$ is the unit outward normal on the boundary $\partial\Omega$. The initial conditions read as

$$(\mathbf{u}, p, \phi, \rho)|_{t=0} = (\mathbf{u}^0, p^0, \phi^0, \rho^0). \tag{2.13}$$

By taking the L^2 inner product of (2.4) with 1, and of (2.6) with 1, one can see the total mass of local density variable ϕ and concentration variable ρ are conserved accurately, i.e.,

$$\frac{d}{dt}\int_\Omega \phi d\boldsymbol{x} = 0,\ \frac{d}{dt}\int_\Omega \rho d\boldsymbol{x} = 0. \tag{2.14}$$

It is straight forward to obtain the PDE energy law for the system (2.4)–(2.9) from the following process. By taking the inner product of (2.4) by μ in L^2, we get

$$(\phi_t, \mu) = -M_1\left\|\mu - \frac{1}{|\Omega|}\int_\Omega \mu d\boldsymbol{x}\right\|^2 - \underbrace{\int_\Omega \nabla\cdot(\mathbf{u}\phi)\mu d\boldsymbol{x}}_{\mathrm{I}}, \tag{2.15}$$

where we use

$$\begin{aligned}&(\mu - \frac{1}{|\Omega|}\int_\Omega \mu d\boldsymbol{x}, \mu)\\ &= (\mu - \frac{1}{|\Omega|}\int_\Omega \mu d\boldsymbol{x}, \mu - \frac{1}{|\Omega|}\int_\Omega \mu d\boldsymbol{x}) + (\mu - \frac{1}{|\Omega|}\int_\Omega \mu d\boldsymbol{x}, \frac{1}{|\Omega|}\int_\Omega \mu d\boldsymbol{x})\\ &= \left\|\mu - \frac{1}{|\Omega|}\int_\Omega \mu d\boldsymbol{x}\right\|^2.\end{aligned} \tag{2.16}$$

By taking the inner product of (2.5) with $-\phi_t$ in L^2 and using integration by parts, we get

$$-(\mu, \phi_t) = -\frac{d}{dt}\int_\Omega \lambda_1(\frac{1}{2}|\nabla\phi|^2 + \frac{1}{\epsilon^2}F(\phi))d\boldsymbol{x} - \int_\Omega W_\phi \phi_t d\boldsymbol{x}. \tag{2.17}$$

Taking the inner product of (2.6) by ω in L^2 and using integration by parts, we obtain

$$(\rho_t, \omega) = -M_2\left\|\omega - \frac{1}{|\Omega|}\int_\Omega \omega d\boldsymbol{x}\right\|^2 - \underbrace{\int_\Omega \nabla\cdot(\mathbf{u}\rho)\omega d\boldsymbol{x}}_{\text{II}}, \tag{2.18}$$

Taking the inner product of (2.5) with $-\rho_t$ in L^2 and using integration by parts, we get

$$-(\omega, \rho_t) = -\frac{d}{dt}\int_\Omega \lambda_2(\frac{\gamma}{2}|\nabla\rho|^2 + \frac{1}{\eta^2}G(\rho))d\boldsymbol{x} - \int_\Omega W_\rho \rho_t d\boldsymbol{x}. \tag{2.19}$$

Taking the inner product of (2.8) with $\mathbf{u}$ in L^2, and using integration by parts and (2.9), we obtain

$$\frac{d}{dt}\int_\Omega \frac{1}{2}|\mathbf{u}|^2 d\boldsymbol{x} + \nu\|\nabla\mathbf{u}\|^2 = \underbrace{-\int_\Omega \phi\nabla\mu\cdot\mathbf{u}d\boldsymbol{x}}_{\text{III}} - \underbrace{\int_\Omega \rho\nabla\omega\cdot\mathbf{u}d\boldsymbol{x}}_{\text{IV}} - \underbrace{\int_\Omega (\mathbf{u}\cdot\nabla)\mathbf{u}\cdot\mathbf{u}d\boldsymbol{x}}_{\text{V}}. \tag{2.20}$$

Combining the above five equations, we derive the energy law as follows:

$$\frac{d}{dt}E(\phi, \rho, \mathbf{u}) = -M_1\left\|\mu - \frac{1}{|\Omega|}\int_\Omega \mu d\boldsymbol{x}\right\|^2 - M_2\left\|\omega - \frac{1}{|\Omega|}\int_\Omega \omega d\boldsymbol{x}\right\|^2 - \nu\|\nabla\mathbf{u}\|^2, \tag{2.21}$$

where terms I and III, II and IV are canceled after using integration by parts, term V vanishes due to the divergence free condition of $\mathbf{u}$. The three negative terms on the right end of (2.21) specify the diffusion rate of the total free energy $E(\phi, \rho, \mathbf{u})$.

Remark 2.2. We notice that in the process of deriving the law of energy (2.21), the three nonlinear terms of advection and surface tensions are all canceled after taking the inner product with some specific functions. In other words, these three terms do not contribute to the total free energy or energy diffusion rate. Therefore, in the next section, we will use such a unique "zero-energy-contribution" feature behind these terms to develop a fully-decoupled scheme.

3. Numerical scheme

In this section, we design a novel method to obtain a linear, stable, fully-decoupled scheme with second-order accuracy. In addition to the projection method (for Navier–Stokes) and the SAV method (for nonlinear potential), the main novelty is the introduction of an ordinary differential equation to achieve explicit processing of the coupling terms. The detailed procedure is as follows.

First, we introduce a nonlocal variable $Q(t)$ and an ODE system related to it that reads as:

$$\begin{cases} Q_t = \displaystyle\int_\Omega \Big(\nabla\cdot(\mathbf{u}\phi)\mu + (\phi\nabla\mu)\cdot\mathbf{u} + \nabla\cdot(\mathbf{u}\rho)\omega + (\rho\nabla\omega)\cdot\mathbf{u} + (\mathbf{u}\cdot\nabla)\mathbf{u}\cdot\mathbf{u}\Big)d\boldsymbol{x},\\ \nabla\cdot\mathbf{u} = 0,\\ Q|_{(t=0)} = 1,\\ \mathbf{u}|_{\partial\Omega} = \mathbf{0} \text{ or all variables are periodic.}\end{cases} \tag{3.1}$$

Using integration by parts, it is easy to derive that the ODE (3.1) is equivalent to a trivial ODE ($Q_t = 0$, $Q|_{(t=0)} = 1$) which has the solution of $Q(t) = 1$.

Second, we define another nonlocal variable $U(t)$ as

$$U = \sqrt{\int_\Omega Z(\phi, \rho) d\boldsymbol{x} + B}, \tag{3.2}$$

where $Z(\phi, \rho) = \lambda_1 \frac{F(\phi)}{\epsilon^2} + \lambda_2 \frac{G(\rho)}{\eta^2} + W(\phi, \rho)$, B is a constant to guarantee the radicand always be positive. We can always find such a constant B since the nonlocal term in the radicand is always bounded from below. (It is easy to see that $-\frac{\theta}{2}\rho|\nabla\phi|^4 \le \frac{\zeta}{4}|\nabla\phi|^4 + c\rho^2$ for some constant c, and $c\rho^2$ can be always bounded by $G(\rho)$. Similar derivation also applies to the θ_2 term.)

Then, by combining the two nonlocal variables Q and U, and the trivial evolution equation (3.1), we rewrite the system (2.4)–(2.9) to the following equivalent form:

$$\phi_t + Q\nabla\cdot(\mathbf{u}\phi) = -M_1\left(\mu - \frac{1}{|\Omega|}\int_\Omega \mu d\boldsymbol{x}\right), \tag{3.3}$$

$$\mu = -\lambda_1 \Delta\phi + HU, \tag{3.4}$$

$$\rho_t + Q\nabla\cdot(\mathbf{u}\rho) = -M_2\left(\omega - \frac{1}{|\Omega|}\int_\Omega \omega d\boldsymbol{x}\right), \tag{3.5}$$

$$\omega = -\lambda_2\gamma\Delta\rho + RU, \tag{3.6}$$

$$U_t = \frac{1}{2}\int_\Omega (H\phi_t + R\rho_t) d\boldsymbol{x}, \tag{3.7}$$

$$\mathbf{u}_t + Q(\mathbf{u}\cdot\nabla)\mathbf{u} + \nabla p - \nu\Delta\mathbf{u} + Q\phi\nabla\mu + Q\rho\nabla\omega = 0, \tag{3.8}$$

$$\nabla\cdot\mathbf{u} = 0, \tag{3.9}$$

$$Q_t = \int_\Omega \Big(\nabla\cdot(\mathbf{u}\phi)\mu + (\phi\nabla\mu)\cdot\mathbf{u} + \nabla\cdot(\mathbf{u}\rho)\omega + (\rho\nabla\omega)\cdot\mathbf{u} + (\mathbf{u}\cdot\nabla)\mathbf{u}\cdot\mathbf{u}\Big) d\boldsymbol{x}, \tag{3.10}$$

where

$$H(\phi, \rho) = \frac{\lambda_1 \frac{f(\phi)}{\epsilon^2} + W_\phi}{\sqrt{\int_\Omega Z(\phi, \rho) d\boldsymbol{x} + B}}, \; R(\phi, \rho) = \frac{\lambda_2 \frac{g(\rho)}{\eta^2} + W_\rho}{\sqrt{\int_\Omega Z(\phi, \rho) d\boldsymbol{x} + B}}. \tag{3.11}$$

The transformed system (3.3)–(3.10) satisfies the following initial conditions,

$$(\mathbf{u}, p, \phi, \rho)|_{t=0} = (\mathbf{u}^0, p^0, \phi^0, \rho^0), \; U|_{t=0} = \sqrt{\int_\Omega Z(\phi^0, \rho^0) d\boldsymbol{x} + B}, \; Q|_{t=0} = 1. \tag{3.12}$$

Note the new system (3.3)–(3.10) is equivalent to the original PDE system (2.4)–(2.9) because nonlinear integrals in (3.10) are just zero, which means $Q \equiv 1$. Meanwhile, the new transformed system (3.3)–(3.10) also follows an energy dissipative law which can be derived by a similar procedure to obtain (2.21). We present the detailed process since the energy stability proof in the discrete level follows the same line.

We multiply the inner product of (3.3) by μ in L^2 and use integration by parts to obtain

$$(\phi_t, \mu) = -M_1\left\|\mu - \frac{1}{|\Omega|}\int_\Omega \mu d\boldsymbol{x}\right\|^2 - \underbrace{Q\int_\Omega \nabla\cdot(\mathbf{u}\phi)\mu d\boldsymbol{x}}_{\text{I}}. \tag{3.13}$$

Taking the inner product of (3.4) with $-\phi_t$ in L^2, we get

$$-(\mu, \phi_t) = -\frac{d}{dt}\int_\Omega \frac{\lambda_1}{2}|\nabla\phi|^2 d\boldsymbol{x} - U\int_\Omega H\phi_t d\boldsymbol{x}. \tag{3.14}$$

Taking the inner product of (3.5) by ω in L^2, we obtain

$$(\rho_t, \omega) = -M_2\left\|\omega - \frac{1}{|\Omega|}\int_\Omega \omega d\boldsymbol{x}\right\|^2 - \underbrace{Q\int_\Omega \nabla\cdot(\mathbf{u}\rho)\omega d\boldsymbol{x}}_{\text{II}}. \tag{3.15}$$

Taking the inner product of (3.6) with $-\rho_t$ in L^2, we get

$$-(\omega, \rho_t) = -\frac{d}{dt}\int_\Omega \frac{\lambda_2\gamma}{2}|\nabla\rho|^2 d\boldsymbol{x} - U\int_\Omega R\rho_t d\boldsymbol{x}. \tag{3.16}$$

By multiplying (3.7) with $2U$, we obtain

$$\frac{d}{dt}|U|^2 = U\int_\Omega H\phi_t d\boldsymbol{x} + U\int_\Omega R\rho_t d\boldsymbol{x}. \tag{3.17}$$

Taking the inner product of (3.8) with $\mathbf{u}$ in L^2, and using integration by parts and (3.9), we obtain

$$\frac{d}{dt}\int_\Omega \frac{1}{2}|\mathbf{u}|^2 d\boldsymbol{x} + \nu\|\nabla\mathbf{u}\|^2 = \underbrace{-Q\int_\Omega \phi\nabla\mu\cdot\mathbf{u}d\boldsymbol{x}}_{\text{III}} \underbrace{-Q\int_\Omega \rho\nabla\omega\cdot\mathbf{u}d\boldsymbol{x}}_{\text{IV}} \underbrace{-Q\int_\Omega (\mathbf{u}\cdot\nabla)\mathbf{u}\cdot\mathbf{u}d\boldsymbol{x}}_{\text{V}}. \tag{3.18}$$

By multiplying (3.10) with q, we obtain

$$\begin{aligned}\frac{d}{dt}\left(\frac{1}{2}|Q|^2\right) = &\underbrace{Q\int_\Omega \nabla\cdot(\mathbf{u}\phi)\mu d\boldsymbol{x}}_{\text{I}_1} + \underbrace{Q\int_\Omega \nabla\cdot(\mathbf{u}\rho)\omega d\boldsymbol{x}}_{\text{II}_1} + \underbrace{Q\int_\Omega \phi\nabla\mu\cdot\mathbf{u}d\boldsymbol{x}}_{\text{III}_1}\\ &+ \underbrace{Q\int_\Omega \rho\nabla\omega\cdot\mathbf{u}d\boldsymbol{x}}_{\text{IV}_1} + \underbrace{Q\int_\Omega (\mathbf{u}\cdot\nabla)\mathbf{u}\cdot\mathbf{u}d\boldsymbol{x}}_{\text{V}_1}.\end{aligned} \tag{3.19}$$

Combining all obtained equalities and noticing all nonlinear coupled terms labeled with Greek letters are canceled, we obtain the energy law described as follows:

$$\frac{d}{dt}E(\mathbf{u}, \phi, \rho, U, Q) = -\nu\|\nabla\mathbf{u}\|^2 - M_1\left\|\mu - \frac{1}{|\Omega|}\int_\Omega \mu d\boldsymbol{x}\right\|^2 - M_2\left\|\omega - \frac{1}{|\Omega|}\int_\Omega \omega d\boldsymbol{x}\right\|^2, \tag{3.20}$$

where

$$E(\mathbf{u}, \phi, \rho, U, Q) = \int_\Omega \left(\frac{1}{2}|\mathbf{u}|^2 + \frac{\lambda_1}{2}|\nabla\phi|^2 + \frac{\lambda_2\gamma}{2}|\nabla\rho|^2\right)d\boldsymbol{x} + |U|^2 + \frac{1}{2}|Q|^2 - B. \tag{3.21}$$

Remark 3.1. The derivation of the law of energy shows the advantage of adding an extra ODE for q to the system. In the original formulation (2.4)–(2.9), the advection term (e.g. term I in (2.15)) and the surface tension term (e.g. term III in (2.18)), cancel each other out. Hence, when designing the algorithm, these two items need to use the same discretization method that leads the coupling type scheme. But in the new formulation, the new terms contained in the q equation can help cancel the original advection and surface tensions, for example, the term I can be canceled by term I_1, term III can be canceled by term III_1. This will give us more degrees of freedom to deal with the coupling terms, to get a fully-decoupled scheme. In addition, since the model is modified to a new form, the discrete energy law will be based on the modified model.

3.1. Numerical scheme

Now, we are ready to develop a numerical scheme. Using the second-order backward differentiation formula (BDF2), a time marching scheme to discretize the new system (3.3)–(3.10) reads as follows.

We compute $\tilde{\mathbf{u}}^{n+1}, \mathbf{u}^{n+1}, p^{n+1}, \phi^{n+1}, \mu^{n+1}, \rho^{n+1}, \omega^{n+1}, U^{n+1}, Q^{n+1}$ by

$$\frac{a\phi^{n+1} - b\phi^n + c\phi^{n-1}}{2\delta t} + Q^{n+1}\nabla\cdot(\mathbf{u}^*\phi^*) = -M_1\left(\mu^{n+1} - \frac{1}{|\Omega|}\int_\Omega \mu^{n+1}d\boldsymbol{x}\right), \tag{3.22}$$

$$\mu^{n+1} = -\lambda_1\Delta\phi^{n+1} + \frac{S_1}{\epsilon^2}(\phi^{n+1} - \phi^*) + H^*U^{n+1}, \tag{3.23}$$

$$\frac{a\rho^{n+1} - b\rho^n + c\rho^{n-1}}{2\delta t} + Q^{n+1}\nabla\cdot(\mathbf{u}^*\rho^*) = -M_2\left(\omega^{n+1} - \frac{1}{|\Omega|}\int_\Omega \omega^{n+1}d\boldsymbol{x}\right), \tag{3.24}$$

$$\omega^{n+1} = -\lambda_2\gamma\Delta\rho^{n+1} + \frac{S_2}{\eta^2}(\rho^{n+1} - \rho^*) + R^*U^{n+1}, \tag{3.25}$$

$$aU^{n+1} - bU^n + cU^{n-1} = \frac{1}{2}\int_\Omega (H^*(a\phi^{n+1} - b\phi^n + c\phi^{n-1}) + R^*(a\rho^{n+1} - b\rho^n + c\rho^{n-1}))d\boldsymbol{x}, \tag{3.26}$$

$$\begin{aligned}\frac{a\tilde{\mathbf{u}}^{n+1} - b\mathbf{u}^n + c\mathbf{u}^{n-1}}{\delta t} + Q^{n+1}(\mathbf{u}^*\cdot\nabla)\mathbf{u}^* + \nabla p^n - \nu\Delta\tilde{\mathbf{u}}^{n+1} \\ + Q^{n+1}\phi^*\nabla\mu^* + Q^{n+1}\rho^*\nabla\omega^* = 0,\end{aligned} \tag{3.27}$$

$$\begin{aligned}\frac{1}{2\delta t}(aQ^{n+1} - bQ^n + cQ^{n-1}) = \int_\Omega \Big(\nabla\cdot(\mathbf{u}^*\phi^*)\mu^{n+1} + (\phi^*\nabla\mu^*)\cdot\tilde{\mathbf{u}}^{n+1} + \nabla\cdot(\mathbf{u}^*\rho^*)\omega^{n+1} \\ + (\rho^*\nabla\omega^*)\cdot\tilde{\mathbf{u}}^{n+1} + (\mathbf{u}^*\cdot\nabla)\mathbf{u}^*\cdot\tilde{\mathbf{u}}^{n+1} \Big)\, d\boldsymbol{x},\end{aligned} \tag{3.28}$$

and

$$\frac{a}{2\delta t}(\mathbf{u}^{n+1} - \tilde{\mathbf{u}}^{n+1}) + \nabla(p^{n+1} - p^n) = 0, \tag{3.29}$$

$$\nabla\cdot\mathbf{u}^{n+1} = 0, \tag{3.30}$$

where

$$\begin{cases} a = 3, b = 4, c = 1, \\ \mathbf{u}^* = 2\mathbf{u}^n - \mathbf{u}^{n-1}, \phi^* = 2\phi^n - \phi^{n-1}, \rho^* = 2\rho^n - \rho^{n-1}, \\ \mu^* = 2\mu^n - \mu^{n-1}, \omega^* = 2\omega^n - \omega^{n-1}, \\ H^* = H(\phi^*, \rho^*), R^* = H(\phi^*, \rho^*), \end{cases} \tag{3.31}$$

and S_1 and S_2 are two pre-specified positive stabilization parameters.

The boundary conditions are either periodic or the following

$$\tilde{\mathbf{u}}^{n+1}|_{\partial\Omega} = \mathbf{0}, \mathbf{u}^{n+1}\cdot\boldsymbol{n}|_{\partial\Omega} = \partial_{\boldsymbol{n}}\phi^{n+1}|_{\partial\Omega} = \partial_{\boldsymbol{n}}\rho^{n+1}|_{\partial\Omega} = 0. \tag{3.32}$$

Remark 3.2. The initialization of the second-order scheme requires all values at $t = t^1$, which can be obtained by constructing the first-order scheme based on the backward Euler method. In the above second-order scheme (3.22)–(3.30), as long as we set $a = 2, b = 2, c = 0$, $\psi^* = \psi^0$ for any variable ψ, the first-order solution can be easily obtained. Moreover, by induction, it is easy to derive that the following volume conservation property holds

$$\int_\Omega \phi^{n+1}d\boldsymbol{x} = \int_\Omega \phi^n d\boldsymbol{x} = \cdots = \int_\Omega \phi^0 d\boldsymbol{x}, \ \int_\Omega \rho^{n+1}d\boldsymbol{x} = \int_\Omega \rho^n d\boldsymbol{x} = \cdots = \int_\Omega \rho^0 d\boldsymbol{x}. \tag{3.33}$$

Remark 3.3. The second-order pressure correction method is adopted here to deal with the Navier–Stokes equations. This method effectively separates the calculation of pressure from that of the velocity field. The scheme is second-order accurate for the velocity but only first-order accurate for pressure, cf. [43]. To obtain the pressure, we just apply the divergence operator to (3.29) and then obtain the following Poisson equation for p^{n+1}, i.e.,

$$-\Delta p^{n+1} = -\frac{3}{2\delta t}\nabla\cdot\tilde{\mathbf{u}}^{n+1} - \Delta p^n. \tag{3.34}$$

Once p^{n+1} is computed from (3.34), we update $\mathbf{u}^{n+1}$ by using (3.29), i.e.,

$$\mathbf{u}^{n+1} = \tilde{\mathbf{u}}^{n+1} - \frac{2\delta t}{3}\nabla(p^{n+1} - p^n). \tag{3.35}$$

Remark 3.4. In the two Allen–Cahn equations of ϕ and ρ, we add two second-order linear stabilization terms related to $S_i, i = 1, 2$ in (3.23) and (3.25) to improve energy stability. Numerical experiments in Section 4 (Figs. 4.2 and 4.3) show that these two stabilizers can effectively improve energy stability when large time steps are used. Moreover, although these two additional stabilizers increase the splitting errors, the increased error is comparable to the error caused by the extrapolation to the nonlinear terms $f(\phi)$ and $g(\rho)$.

3.2. Implementation process

It appears that all unknown variables are nonlocally coupled together, and thus the developed scheme (3.22)–(3.30) is not the fully-decoupled scheme that we expect. This reminds us that we cannot use the direct

iteration method to solve it because doing so will cause a lot of time consumption. Next, we detail the implementation process, in which we make full use of the nonlocal characteristics of the two addition variables U, q, as shown below.

First, we rewrite (3.26) to the following form

$$U^{n+1} = \frac{1}{2}\int_{\Omega}(H^*\phi^{n+1} + R^*\rho^{n+1})d\boldsymbol{x} + g^n, \tag{3.36}$$

where

$$g^n = \frac{bU^n - cU^{n-1}}{a} - \frac{1}{2}\int_{\Omega}(H^*\frac{b\phi^n - c\phi^{n-1}}{a} + R^*\frac{b\rho^n - c\rho^{n-1}}{a})d\boldsymbol{x}. \tag{3.37}$$

Using (3.36), the system (3.22)–(3.25) becomes

$$\begin{cases} \dfrac{a}{2M_1\delta t}\phi^{n+1} + \dfrac{1}{M_1}Q^{n+1}\nabla\cdot(\mathbf{u}^*\phi^*) = -\Big(\mu^{n+1} - \dfrac{1}{|\Omega|}\displaystyle\int_{\Omega}\mu^{n+1}d\boldsymbol{x}\Big) + \dfrac{b\phi^n - c\phi^{n-1}}{2M_1\delta t}, \\ \mu^{n+1} = \Big(-\lambda_1\Delta + \dfrac{S_1}{\epsilon^2}\Big)\phi^{n+1} + \dfrac{1}{2}H^*\displaystyle\int_{\Omega}(H^*\phi^{n+1} + R^*\rho^{n+1})d\boldsymbol{x} + \Big(g^nH^* - \dfrac{S_1}{\epsilon^2}\phi^*\Big), \\ \dfrac{a}{2M_2\delta t}\rho^{n+1} + \dfrac{1}{M_2}Q^{n+1}\nabla\cdot(\mathbf{u}^*\rho^*) = -\Big(\omega^{n+1} - \dfrac{1}{|\Omega|}\displaystyle\int_{\Omega}\omega^{n+1}d\boldsymbol{x}\Big) + \dfrac{b\rho^n - c\rho^{n-1}}{2M_2\delta t}, \\ \omega^{n+1} = \Big(-\lambda_2\gamma\Delta + \dfrac{S_2}{\eta^2}\Big)\rho^{n+1} + \dfrac{1}{2}R^*\displaystyle\int_{\Omega}(H^*\phi^{n+1} + R^*\rho^{n+1})d\boldsymbol{x} + \Big(g^nR^* - \dfrac{S_2}{\eta^2}\rho^*\Big). \end{cases} \tag{3.38}$$

Second, we use the nonlocal scalar variable Q^{n+1} to split $(\phi, \rho, \mu, \omega)^{n+1}$ into a linear combination that reads as

$$\begin{cases} \phi^{n+1} = \phi_1^{n+1} + Q^{n+1}\phi_2^{n+1}, \quad \mu^{n+1} = \mu_1^{n+1} + Q^{n+1}\mu_2^{n+1}, \\ \rho^{n+1} = \rho_1^{n+1} + Q^{n+1}\rho_2^{n+1}, \quad \omega^{n+1} = \omega_1^{n+1} + Q^{n+1}\omega_2^{n+1}. \end{cases} \tag{3.39}$$

Hence the system (3.38) becomes

$$\begin{cases} \dfrac{a}{2M_1\delta t}(\phi_1^{n+1} + Q^{n+1}\phi_2^{n+1}) + \dfrac{1}{M_1}Q^{n+1}\nabla\cdot(\mathbf{u}^*\phi^*) \\ \qquad = -\left(\mu_1^{n+1} + Q^{n+1}\mu_2^{n+1} - \dfrac{1}{|\Omega|}\displaystyle\int_{\Omega}(\mu_1^{n+1} + Q^{n+1}\mu_2^{n+1})d\boldsymbol{x}\right) + \dfrac{b\phi^n - c\phi^{n-1}}{2M_1\delta t}, \\ \mu_1^{n+1} + Q^{n+1}\mu_2^{n+1} = \Big(-\lambda_1\Delta + \dfrac{S_1}{\epsilon^2}\Big)(\phi_1^{n+1} + Q^{n+1}\phi_2^{n+1}) \\ \qquad + \dfrac{1}{2}H^*\displaystyle\int_{\Omega}(H^*(\phi_1^{n+1} + Q^{n+1}\phi_2^{n+1}) + R^*(\rho_1^{n+1} + Q^{n+1}\rho_2^{n+1}))d\boldsymbol{x} \\ \qquad + \Big(g^nH^* - \dfrac{S_1}{\epsilon^2}\phi^*\Big), \\ \dfrac{a}{2M_2\delta t}(\rho_1^{n+1} + Q^{n+1}\rho_2^{n+1}) + \dfrac{1}{M_2}Q^{n+1}\nabla\cdot(\mathbf{u}^*\rho^*) \\ \qquad = -\left(\omega_1^{n+1} + Q^{n+1}\omega_2^{n+1} - \dfrac{1}{|\Omega|}\displaystyle\int_{\Omega}(\omega_1^{n+1} + Q^{n+1}\omega_2^{n+1})d\boldsymbol{x}\right) + \dfrac{b\rho^n - c\rho^{n-1}}{2M_2\delta t}, \\ \omega_1^{n+1} + Q^{n+1}\omega_2^{n+1} = \Big(-\lambda_2\gamma\Delta + \dfrac{S_2}{\eta^2}\Big)(\rho_1^{n+1} + Q^{n+1}\rho_2^{n+1}) \\ \qquad + \dfrac{1}{2}R^*\displaystyle\int_{\Omega}(H^*(\phi_1^{n+1} + Q^{n+1}\phi_2^{n+1}) + R^*(\rho_1^{n+1} + Q^{n+1}\rho_2^{n+1}))d\boldsymbol{x} \\ \qquad + \Big(g^nR^* - \dfrac{S_2}{\eta^2}\rho^*\Big). \end{cases} \tag{3.40}$$

According to Q^{n+1}, the linear system (3.40) can be decomposed into two sub-systems as follows:

$$\begin{cases} \dfrac{a}{2M_1\delta t}\phi_1^{n+1} = -\Big(\mu_1^{n+1} - \dfrac{1}{|\Omega|}\displaystyle\int_\Omega \mu_1^{n+1}d\boldsymbol{x}\Big) + A_1, \\ \mu_1^{n+1} = \Big(-\lambda_1\Delta + \dfrac{S_1}{\epsilon^2}\Big)\phi_1^{n+1} + \dfrac{1}{2}H^*\displaystyle\int_\Omega (H^*\phi_1^{n+1} + R^*\rho_1^{n+1}) + B_1, \\ \dfrac{a}{2M_2\delta t}\rho_1^{n+1} = -\Big(\omega_1^{n+1} - \dfrac{1}{|\Omega|}\displaystyle\int_\Omega \omega_1^{n+1}d\boldsymbol{x}\Big) + C_1, \\ \omega_1^{n+1} = \Big(-\lambda_2\gamma\Delta + \dfrac{S_2}{\eta^2}\Big)\rho_1^{n+1} + \dfrac{1}{2}R^*\displaystyle\int_\Omega (H^*\phi_1^{n+1} + R^*\rho_1^{n+1})d\boldsymbol{x} + D_1, \end{cases} \tag{3.41}$$

$$\begin{cases} \dfrac{a}{2M_1\delta t}\phi_2^{n+1} = -\Big(\mu_2^{n+1} - \dfrac{1}{|\Omega|}\displaystyle\int_\Omega \mu_2^{n+1}d\boldsymbol{x}\Big) + A_2, \\ \mu_2^{n+1} = \Big(-\lambda_1\Delta + \dfrac{S_1}{\epsilon^2}\Big)\phi_2^{n+1} + \dfrac{1}{2}H^*\displaystyle\int_\Omega (H^*\phi_2^{n+1} + R^*\rho_2^{n+1})d\boldsymbol{x} + B_2, \\ \dfrac{a}{2M_2\delta t}\rho_2^{n+1} = -\Big(\omega_2^{n+1} - \dfrac{1}{|\Omega|}\displaystyle\int_\Omega \omega_2^{n+1}d\boldsymbol{x}\Big)d\boldsymbol{x} + C_2, \\ \omega_2^{n+1} = \Big(-\lambda_2\gamma\Delta + \dfrac{S_2}{\eta^2}\Big)\rho_2^{n+1} + \dfrac{1}{2}R^*\displaystyle\int_\Omega (H^*\phi_2^{n+1} + R^*\rho_2^{n+1})d\boldsymbol{x} + D_2, \end{cases} \tag{3.42}$$

where $A_i, B_i, C_i, D_i, i = 1, 2$ are given explicit forms that read as

$$\begin{cases} A_1 = \dfrac{1}{2M_1\delta t}(b\phi^n - c\phi^{n-1}),\ B_1 = g^n H^* - \dfrac{S_1}{\epsilon^2}\phi^*, \\ C_1 = \dfrac{1}{2M_2\delta t}(b\rho^n - c\rho^{n-1}),\ D_1 = g^n R^* - \dfrac{S_2}{\eta^2}\rho^*, \\ A_2 = -\dfrac{1}{M_1}\nabla\cdot(\mathbf{u}^*\phi^*),\ B_2 = 0,\ C_2 = -\dfrac{1}{M_2}\nabla\cdot(\mathbf{u}^*\rho^*),\ D_2 = 0. \end{cases}$$

The boundary conditions of the two sub-systems (3.41) and (3.42) are either periodic or satisfy

$$\partial_{\mathbf{n}}(\phi_1^{n+1}, \rho_1^{n+1}, \phi_2^{n+1}, \rho_2^{n+1})|_{\partial\Omega} = 0. \tag{3.43}$$

Although the two independent subsystems (3.41) and (3.42) are linear, they are not easy to solve due to the nonlocal nature. Note that the two subsystems (3.41) and (3.42) have the same form except for the explicit source terms $(A, B, C, D)_i, i = 1, 2$, so we only need to introduce a method to solve any one of them, the other follows the same process.

We choose the first subsystem (3.41) as an example to show how to obtain fast calculations. By taking the L^2 inner product with 1 for the first and third equations in (3.41) and using (3.33), we derive

$$\begin{aligned} \int_\Omega \phi_1^{n+1}d\boldsymbol{x} &= \int_\Omega \phi^n d\boldsymbol{x} = \cdots = \int_\Omega \phi^0 d\boldsymbol{x}, \\ \int_\Omega \rho_1^{n+1}d\boldsymbol{x} &= \int_\Omega \rho^n d\boldsymbol{x} = \cdots = \int_\Omega \rho^0 d\boldsymbol{x}. \end{aligned} \tag{3.44}$$

Similarly, from (3.42), we derive

$$\int_\Omega \phi_2^{n+1}d\boldsymbol{x} = 0,\ \int_\Omega \rho_2^{n+1}d\boldsymbol{x} = 0. \tag{3.45}$$

We combine the first two equations and the last two equations in the system (3.41) separately to obtain the following form:

$$\begin{cases} \mathscr{P}(\phi_1^{n+1}) + \dfrac{1}{2}\bar{H}^*\displaystyle\int_\Omega (H^*\phi_1^{n+1} + R^*\rho_1^{n+1})d\boldsymbol{x} = \chi_1, \\ \mathscr{Q}(\rho_1^{n+1}) + \dfrac{1}{2}\bar{R}^*\displaystyle\int_\Omega (H^*\phi_1^{n+1} + R^*\rho_1^{n+1})d\boldsymbol{x} = \chi_2, \end{cases} \tag{3.46}$$

where

$$\begin{cases} \mathscr{P}(\phi) = \dfrac{a}{2M_1\delta t}\phi - \lambda_1\Delta\phi + \dfrac{S_1}{\epsilon^2}\phi, \\ \mathscr{Q}(\rho) = \dfrac{a}{2M_2\delta t}\rho - \lambda_2\gamma\Delta\rho + \dfrac{S_2}{\eta^2}\rho, \\ \bar{H}^* = H^* - \dfrac{1}{|\Omega|}\displaystyle\int_\Omega H^* d\boldsymbol{x}, \bar{R}^* = R^* - \dfrac{1}{|\Omega|}\int_\Omega R^* d\boldsymbol{x}, \\ \chi_1 = g^n H^* - \dfrac{1}{|\Omega|}\displaystyle\int_\Omega g^n H^* d\boldsymbol{x} - \dfrac{S_1}{\epsilon^2}\phi^* + \dfrac{1}{2M_1\delta t}(b\phi^n - c\phi^{n-1}), \\ \chi_2 = g^n R^* - \dfrac{1}{|\Omega|}\displaystyle\int_\Omega g^n R^* d\boldsymbol{x} - \dfrac{S_2}{\eta^2}\rho^* + \dfrac{1}{2M_2\delta t}(b\rho^n - c\rho^{n-1}). \end{cases} \tag{3.47}$$

We define the linear operator $\mathscr{P}^{-1}$ and $\mathscr{Q}^{-1}$ such that for any function $v_1, v_2 \in L^2(\Omega)$,

$$\begin{aligned} &u_1 = \mathscr{P}^{-1}(v_1) : \mathscr{P}(u_1) = v_1; \\ &u_2 = \mathscr{Q}^{-1}(v_2) : \mathscr{Q}(u_2) = v_2. \end{aligned} \tag{3.48}$$

By applying $\mathscr{P}^{-1}$ and $\mathscr{Q}^{-1}$ to the two equations in (3.46) respectively, we derive

$$\begin{cases} \phi_1^{n+1} + \dfrac{1}{2}\mathscr{P}^{-1}(\bar{H}^*)\displaystyle\int_\Omega (H^*\phi_1^{n+1} + R^*\rho_1^{n+1}) d\boldsymbol{x} = \mathscr{P}^{-1}(\chi_1), \\ \rho_1^{n+1} + \dfrac{1}{2}\mathscr{Q}^{-1}(\bar{R}^*)\displaystyle\int_\Omega (H^*\phi_1^{n+1} + R^*\rho_1^{n+1}) d\boldsymbol{x} = \mathscr{Q}^{-1}(\chi_2). \end{cases} \tag{3.49}$$

After multiplying the L^2 inner product with H^* and R^* for the above two equations respectively, we derive the following linear system

$$\begin{bmatrix} 1+\alpha & \alpha \\ \beta & 1+\beta \end{bmatrix} \begin{bmatrix} \int_\Omega H^*\phi_1^{n+1} d\boldsymbol{x} \\ \int_\Omega R^*\rho_1^{n+1} d\boldsymbol{x} \end{bmatrix} = \begin{bmatrix} \int_\Omega H^*\mathscr{P}^{-1}(\chi_1) d\boldsymbol{x} \\ \int_\Omega R^*\mathscr{Q}^{-1}(\chi_2) d\boldsymbol{x} \end{bmatrix}, \tag{3.50}$$

where

$$\alpha = \frac{1}{2}\int_\Omega H^*\mathscr{P}^{-1}(\bar{H}^*) d\boldsymbol{x}, \quad \beta = \int_\Omega R^*\mathscr{Q}^{-1}(\bar{R}^*) d\boldsymbol{x}. \tag{3.51}$$

The determinant of the 2×2 matrix in (3.50) is $1 + \alpha + \beta$ which can be verified to be non-zero by the following process. Suppose $\psi = \mathscr{P}^{-1}(\bar{H}^*)$, then ψ satisfies

$$\mathscr{P}(\psi) = \bar{H}^*. \tag{3.52}$$

By taking the L^2 inner product of (3.52) with 1, we obtain

$$\int_\Omega \psi d\boldsymbol{x} = 0. \tag{3.53}$$

Furthermore, by taking the L^2 inner product of (3.52) with ψ and using (3.53), we derive

$$\alpha = \int_\Omega H^*\psi d\boldsymbol{x} = \left(\frac{a}{2M_1\delta t} + \frac{S_1}{\epsilon^2}\right)\|\psi\|^2 + \lambda_1\|\nabla\psi\|^2 \geq 0. \tag{3.54}$$

Similarly, we also have $\beta \geq 0$. This implies the matrix system (3.50) is uniquely solvable. After obtaining the two nonlocal terms $\int_\Omega H^*\phi_1^{n+1} d\boldsymbol{x}$ and $\int_\Omega R^*\rho_1^{n+1} d\boldsymbol{x}$ from (3.50), we can obtain ϕ_1^{n+1} and ρ_1^{n+1} from (3.49). By using the similar process to the linear system (3.42), one can obtain ϕ_2^{n+1} and ρ_2^{n+1}.

Third, for the velocity field $\tilde{\mathbf{u}}^{n+1}, \mathbf{u}^{n+1}$ and the pressure p^{n+1} in the scheme (3.27) and (3.29)–(3.30), we also use the nonlocal variable Q^{n+1} to split them as the following linear combinations:

$$\begin{cases} \tilde{\mathbf{u}}^{n+1} = \tilde{\mathbf{u}}_1^{n+1} + Q^{n+1}\tilde{\mathbf{u}}_2^{n+1}, \\ \mathbf{u}^{n+1} = \mathbf{u}_1^{n+1} + Q^{n+1}\mathbf{u}_2^{n+1}, \\ p^{n+1} = p_1^{n+1} + Q^{n+1}p_2^{n+1}. \end{cases} \tag{3.55}$$

By replacing these variables $\tilde{\mathbf{u}}^{n+1}$, $\mathbf{u}^{n+1}$, p^{n+1} in the scheme (3.27) and (3.29)–(3.30), and then splitting the obtained equations according to Q^{n+1}, we arrive at a system that includes two sub-equations for each variable. More precisely, from (3.27), the two split variables $\tilde{\mathbf{u}}_i^{n+1}, i = 1, 2$ follow the equations:

$$\begin{cases} \dfrac{a}{2\delta t}\tilde{\mathbf{u}}_1^{n+1} - \nu\Delta\tilde{\mathbf{u}}_1^{n+1} = \sigma_1, \\ \dfrac{a}{2\delta t}\tilde{\mathbf{u}}_2^{n+1} - \nu\Delta\tilde{\mathbf{u}}_2^{n+1} = \sigma_2, \end{cases} \tag{3.56}$$

where

$$\sigma_1 = -\nabla p^n + \frac{b\mathbf{u}^n - c\mathbf{u}^{n-1}}{2\delta t}, \quad \sigma_2 = -(\mathbf{u}^*\cdot\nabla)\mathbf{u}^* - \phi^*\nabla\mu^* - \rho^*\nabla\omega^*, \tag{3.57}$$

are all explicit forms. Similarly, from (3.29)–(3.30), the two split variables $\mathbf{u}_i^{n+1}$, $p_i^{n+1}, i = 1, 2$ follow the equations:

$$\begin{cases} \dfrac{3}{2\delta t}(\mathbf{u}_1^{n+1} - \tilde{\mathbf{u}}_1^{n+1}) + \nabla p_1^{n+1} = \Upsilon_1, \quad \nabla\cdot\mathbf{u}_1^{n+1} = 0, \\ \dfrac{3}{2\delta t}(\mathbf{u}_2^{n+1} - \tilde{\mathbf{u}}_2^{n+1}) + \nabla p_2^{n+1} = \Upsilon_2, \quad \nabla\cdot\mathbf{u}_2^{n+1} = 0, \end{cases} \tag{3.58}$$

where $\Upsilon_1 = \nabla p^n$ and $\Upsilon_2 = 0$ are explicit forms as well. We request the four split variables $\tilde{\mathbf{u}}_i^{n+1}, \mathbf{u}_i^{n+1}, i = 1, 2$ follow the boundary conditions described in (3.32), i.e, they are either periodic or satisfy:

$$\tilde{\mathbf{u}}_i^{n+1}|_{\partial\Omega} = \mathbf{0}, \mathbf{u}_i^{n+1}\cdot\boldsymbol{n}|_{\partial\Omega} = 0. \tag{3.59}$$

Fourth, we solve the auxiliary variable Q^{n+1}. Using the split form for the variables $\mu^{n+1}, \omega^{n+1}, \tilde{\mathbf{u}}^{n+1}$, one can rewrite (3.28) as the following form:

$$(\frac{a}{2\delta t} - \vartheta_2)Q^{n+1} = \frac{1}{2\delta t}(bQ^n - cQ^{n-1}) + \vartheta_1, \tag{3.60}$$

where

$$\begin{aligned} \vartheta_i = \int_\Omega \Big(&\nabla\cdot(\mathbf{u}^*\phi^*)\mu_i^{n+1} + (\phi^*\nabla\mu^*)\cdot\tilde{\mathbf{u}}_i^{n+1} \\ &+ \nabla\cdot(\mathbf{u}^*\rho^*)\omega_i^{n+1} + (\rho^*\nabla\omega^*)\cdot\tilde{\mathbf{u}}_i^{n+1} + (\mathbf{u}^*\cdot\nabla)\mathbf{u}^*\cdot\tilde{\mathbf{u}}_i^{n+1} \Big)\, d\boldsymbol{x}, i = 1, 2. \end{aligned} \tag{3.61}$$

We need to verify whether (3.60) is solvable or not. By multiplying the L^2 inner product of the second equation in (3.56) with $\tilde{\mathbf{u}}_2^{n+1}$, we get

$$\begin{aligned} &-\int_\Omega \Big((\mathbf{u}^*\cdot\nabla)\mathbf{u}^*\cdot\tilde{\mathbf{u}}_2^{n+1} + (\phi^*\nabla\mu^*)\cdot\tilde{\mathbf{u}}_2^{n+1} + (\rho^*\nabla\omega^*)\cdot\tilde{\mathbf{u}}_2^{n+1}\Big) \\ &= \frac{a}{2\delta t}\|\tilde{\mathbf{u}}_2^{n+1}\|^2 + \nu\|\nabla\tilde{\mathbf{u}}_2^{n+1}\|^2 \geq 0. \end{aligned} \tag{3.62}$$

By taking the L^2 inner product of the first equation in (3.42) with $M_1\mu_2^{n+1}$, of the second equation with $-\frac{a}{2\delta t}\phi_2^{n+1}$, of the third equation with $M_2\omega_2^{n+1}$, of the fourth equation with $-\frac{a}{2\delta t}\rho_2^{n+1}$, and combining all obtained equations, we derive

$$\begin{aligned} &-\int_\Omega (\nabla\cdot(\mathbf{u}^*\phi^*)\mu_2^{n+1} + \nabla\cdot(\mathbf{u}^*\rho^*)\omega_2^{n+1})d\boldsymbol{x} \\ &= M_1\left\|\mu_2^{n+1} - \frac{1}{|\Omega|}\int_\Omega \mu_2^{n+1}d\boldsymbol{x}\right\|^2 + M_2\left\|\omega_2^{n+1} - \frac{1}{|\Omega|}\int_\Omega \omega_2^{n+1}d\boldsymbol{x}\right\|^2 \\ &\quad + \frac{a}{2\delta t}\lambda_1\|\nabla\phi_2^{n+1}\|^2 + \frac{aS_1}{2\delta t\epsilon^2}\|\phi_2^{n+1}\|^2 + \frac{a}{2\delta t}\lambda_2\gamma\|\nabla\rho_2^{n+1}\|^2 + \frac{aS_2}{2\delta t\eta^2}\|\rho_2^{n+1}\|^2 \\ &\quad + \frac{1}{2}\left(\int_\Omega H^*\phi_2^{n+1}d\boldsymbol{x} + \int_\Omega R^*\rho_2^{n+1}d\boldsymbol{x}\right)^2 \geq 0. \end{aligned} \tag{3.63}$$

This implies $-\vartheta_2 \geq 0$ and the solvability of (3.60) is verified.

Finally, we update ϕ^{n+1}, ρ^{n+1}, μ^{n+1}, ω^{n+1} from (3.39), $\tilde{\mathbf{u}}^{n+1}$, $\mathbf{u}^{n+1}$, and p^{n+1} from (3.55), and U^{n+1} from (3.36).

In summary, the scheme (3.22)–(3.30) can be implemented in the following way:

- *Step 1*: Compute $\int_\Omega H^*\phi_1^{n+1}d\boldsymbol{x}$, $\int_\Omega R^*\rho_1^{n+1}d\boldsymbol{x}$ from (3.50), and $\int_\Omega H^*\phi_2^{n+1}d\boldsymbol{x}$, $\int_\Omega R^*\rho_2^{n+1}d\boldsymbol{x}$ from another similar matrix system derived from (3.42);
- *Step 2*: Update ϕ_1^{n+1}, ρ_1^{n+1} from (3.49); and update ϕ_2^{n+1}, ρ_2^{n+1} from another similar equality derived from (3.42);
- *Step 3*: Compute $\tilde{\mathbf{u}}_i$, $i = 1, 2$ from (3.56);
- *Step 4*: Compute $\mathbf{u}_i$ and p_i, $i = 1, 2$ from (3.58) (see Remark 3.3);
- *Step 5*: Compute Q^{n+1} from (3.60);
- *Step 6*: Update ϕ^{n+1}, ρ^{n+1}, μ^{n+1}, ω^{n+1} from (3.39), $\tilde{\mathbf{u}}^{n+1}$, $\mathbf{u}^{n+1}$, and p^{n+1} from (3.55), and U^{n+1} from (3.36).

Hence, the total cost of solving the (3.22)–(3.30) at each time step includes the six independent linear elliptic equations in Step 1 ($\mathscr{P}^{-1}(\chi_1)$, $\mathscr{Q}^{-1}(\chi_2)$, $\mathscr{P}^{-1}(\bar{H}^*)$, $\mathscr{Q}^{-1}(\bar{R}^*)$ and other two derived from (3.42)), two elliptic type equations in Step 3, and two other Poisson type equations in Step 4. All these equations have constant coefficients and are completely decoupled, which means very effective calculations in practice.

The following theorem ensures that the developed scheme (3.22)–(3.30) satisfies the energy stability unconditionally.

Theorem 3.1. *The following discrete energy dissipation law holds for the scheme (3.22)–(3.30),*

$$\begin{aligned}\frac{1}{\delta t}(E^{n+1}-E^{n-1}) \le & -\nu\|\nabla\tilde{\mathbf{u}}^{n+1}\|^2 - M_1\left\|\mu^{n+1}-\frac{1}{|\Omega|}\int_\Omega \mu^{n+1}d\boldsymbol{x}\right\|^2 \\ & - M_2\left\|\omega^{n+1}-\frac{1}{|\Omega|}\int_\Omega \omega^{n+1}d\boldsymbol{x}\right\|^2 \le 0,\end{aligned} \tag{3.64}$$

where

$$\begin{aligned}E^{n+1} =& \frac{1}{2}\Big(\frac{1}{2}\|\mathbf{u}^{n+1}\|^2+\frac{1}{2}\|2\mathbf{u}^{n+1}-\mathbf{u}^n\|^2\Big)+\frac{\lambda_1}{2}\Big(\frac{1}{2}\|\nabla\phi^{n+1}\|^2+\frac{1}{2}\|2\nabla\phi^{n+1}-\nabla\phi^n\|^2\Big) \\ &+\frac{\lambda_2\gamma}{2}\Big(\frac{1}{2}\|\nabla\rho^{n+1}\|^2+\frac{1}{2}\|2\nabla\rho^{n+1}-\nabla\rho^n\|^2\Big)+\Big(\frac{1}{2}|U^{n+1}|^2+\frac{1}{2}|2U^{n+1}-U^n|^2\Big) \\ &+\frac{1}{2}\Big(\frac{1}{2}|Q^{n+1}|^2+\frac{1}{2}|2Q^{n+1}-Q^n|^2\Big)+\frac{\delta t^2}{3}\|\nabla p^{n+1}\|^2 \\ &+\frac{S_1}{2\epsilon^2}\|\phi^{n+1}-\phi^n\|^2+\frac{S_2}{2\eta^2}\|\rho^{n+1}-\rho^n\|^2.\end{aligned} \tag{3.65}$$

Proof. We multiply the inner product of (3.27) with $2\delta t\tilde{\mathbf{u}}^{n+1}$ in the L^2 space, we obtain

$$\begin{aligned}&(3\tilde{\mathbf{u}}^{n+1}-4\mathbf{u}^n+\mathbf{u}^{n-1},\tilde{\mathbf{u}}^{n+1})+2\nu\delta t\|\nabla\tilde{\mathbf{u}}^{n+1}\|^2+2\delta t(\nabla p^n,\tilde{\mathbf{u}}^{n+1}) \\ &+2\delta t\,Q^{n+1}\int_\Omega(\mathbf{u}^*\cdot\nabla)\mathbf{u}^*\cdot\tilde{\mathbf{u}}^{n+1}d\boldsymbol{x}++2\delta t\,Q^{n+1}\int_\Omega\phi^*\nabla\mu^*\cdot\tilde{\mathbf{u}}^{n+1}d\boldsymbol{x} \\ &+2\delta t\,Q^{n+1}\int_\Omega\rho^*\nabla\omega^*\cdot\tilde{\mathbf{u}}^{n+1}d\boldsymbol{x}=0.\end{aligned} \tag{3.66}$$

From (3.29), for any variable $\boldsymbol{v}$ with $\nabla\cdot\boldsymbol{v}=0$, we have

$$(\mathbf{u}^{n+1},\boldsymbol{v})=(\tilde{\mathbf{u}}^{n+1},\boldsymbol{v}). \tag{3.67}$$

We derive following equality

$$\begin{aligned}
&(3\tilde{\mathbf{u}}^{n+1}-4\mathbf{u}^{n}+\mathbf{u}^{n-1},\tilde{\mathbf{u}}^{n+1})\\
&\quad=(3\tilde{\mathbf{u}}^{n+1}-4\mathbf{u}^{n}+\mathbf{u}^{n-1},\mathbf{u}^{n+1})+(3\tilde{\mathbf{u}}^{n+1}-4\mathbf{u}^{n}+\mathbf{u}^{n-1},\tilde{\mathbf{u}}^{n+1}-\mathbf{u}^{n+1})\\
&\quad=(3\mathbf{u}^{n+1}-4\mathbf{u}^{n}+\mathbf{u}^{n-1},\mathbf{u}^{n+1})+(3\tilde{\mathbf{u}}^{n+1},\ \tilde{\mathbf{u}}^{n+1}-\mathbf{u}^{n+1})\\
&\quad=(3\mathbf{u}^{n+1}-4\mathbf{u}^{n}+\mathbf{u}^{n-1},\mathbf{u}^{n+1})+3(\tilde{\mathbf{u}}^{n+1}-\mathbf{u}^{n+1},\tilde{\mathbf{u}}^{n+1}+\mathbf{u}^{n+1})\\
&\quad=\frac{1}{2}\Big(\|\mathbf{u}^{n+1}\|^2-\|\mathbf{u}^{n}\|^2+\|2\mathbf{u}^{n+1}-\mathbf{u}^{n}\|^2-\|2\mathbf{u}^{n}-\mathbf{u}^{n-1}\|^2\\
&\qquad+\|\mathbf{u}^{n+1}-2\mathbf{u}^{n}+\mathbf{u}^{n-1}\|^2\Big)+3(\|\tilde{\mathbf{u}}^{n+1}\|^2-\|\mathbf{u}^{n+1}\|^2),
\end{aligned}\tag{3.68}$$

where we use the following identity

$$2(3a-4b+c,a)=a^2-b^2+(2a-b)^2-(2b-c)^2+(a-2b+c)^2.\tag{3.69}$$

We reformulate the projection step (3.29) as

$$\frac{3}{2\delta t}\mathbf{u}^{n+1}+\nabla p^{n+1}=\frac{3}{2\delta t}\tilde{\mathbf{u}}^{n+1}+\nabla p^{n}.\tag{3.70}$$

By taking the square of both sides of the above equation, we get

$$\frac{9}{4\delta t^2}\|\mathbf{u}^{n+1}\|^2+\|\nabla p^{n+1}\|^2=\frac{9}{4\delta t^2}\|\tilde{\mathbf{u}}^{n+1}\|^2+\|\nabla p^{n}\|^2+\frac{3}{\delta t}(\tilde{\mathbf{u}}^{n+1},\nabla p^{n}).\tag{3.71}$$

Hence, by multiplying $2\delta t^2/3$ of the above equation, we derive

$$\frac{3}{2}(\|\mathbf{u}^{n+1}\|^2-\|\tilde{\mathbf{u}}^{n+1}\|^2)+\frac{2\delta t^2}{3}(\|\nabla p^{n+1}\|^2-\|\nabla p^{n}\|^2)=2\delta t(\tilde{\mathbf{u}}^{n+1},\nabla p^{n}).\tag{3.72}$$

By taking the inner product of (3.29) with $2\delta t\mathbf{u}^{n+1}$ in the L^2 space, we have

$$\frac{3}{2}(\|\mathbf{u}^{n+1}\|^2-\|\tilde{\mathbf{u}}^{n+1}\|^2+\|\mathbf{u}^{n+1}-\tilde{\mathbf{u}}^{n+1}\|^2)=0.\tag{3.73}$$

We combine (3.66), (3.68), (3.72), and (3.73) to obtain

$$\begin{aligned}
&\frac{1}{2}(\|\mathbf{u}^{n+1}\|^2-\|\mathbf{u}^{n}\|^2+\|2\mathbf{u}^{n+1}-\mathbf{u}^{n}\|^2-\|2\mathbf{u}^{n}-\mathbf{u}^{n-1}\|^2+\|\mathbf{u}^{n+1}-2\mathbf{u}^{n}+\mathbf{u}^{n-1}\|^2)\\
&\quad+\frac{3}{2}\|\mathbf{u}^{n+1}-\tilde{\mathbf{u}}^{n+1}\|^2+\frac{2\delta t^2}{3}(\|\nabla p^{n+1}\|^2-\|\nabla p^{n}\|^2)+2\nu\delta t\|\nabla\tilde{\mathbf{u}}^{n+1}\|^2\\
&\quad+2\delta t\,Q^{n+1}\int_\Omega(\mathbf{u}^{*}\cdot\nabla)\mathbf{u}^{*}\cdot\tilde{\mathbf{u}}^{n+1}d\boldsymbol{x}+2\delta t\,Q^{n+1}\int_\Omega\phi^{*}\nabla\mu^{*}\cdot\tilde{\mathbf{u}}^{n+1}d\boldsymbol{x}\\
&\quad+2\delta t\,Q^{n+1}\int_\Omega\rho^{*}\nabla\omega^{*}\cdot\tilde{\mathbf{u}}^{n+1}d\boldsymbol{x}=0.
\end{aligned}\tag{3.74}$$

Computing the inner product of (3.22) with $2\delta t\mu^{n+1}$ in the L^2 space, we have

$$\begin{aligned}
&(3\phi^{n+1}-4\phi^{n}+\phi^{n-1},\mu^{n+1})+2\delta t\,Q^{n+1}\int_\Omega\nabla\cdot(\mathbf{u}^{*}\phi^{*})\mu^{n+1}d\boldsymbol{x}\\
&\qquad+2\delta t\,M_1\left\|\mu^{n+1}-\frac{1}{|\Omega|}\int_\Omega\mu^{n+1}d\boldsymbol{x}\right\|^2=0.
\end{aligned}\tag{3.75}$$

Computing the L^2 inner product of (3.23) with $-(3\phi^{n+1}-4\phi^{n}+\phi^{n-1})$, we find

$$\begin{aligned}
&-(\mu^{n+1},3\phi^{n+1}-4\phi^{n}+\phi^{n-1})+\lambda_1(\nabla\phi^{n+1},\nabla(3\phi^{n+1}-4\phi^{n}+\phi^{n-1}))\\
&\qquad+U^{n+1}\int_\Omega H^{*}(3\phi^{n+1}-4\phi^{n}+\phi^{n-1})d\boldsymbol{x}\\
&\qquad+\frac{S_1}{\epsilon^2}(\phi^{n+1}-\phi^{*},3\phi^{n+1}-4\phi^{n}+\phi^{n-1})=0.
\end{aligned}\tag{3.76}$$

Computing the inner product of (3.24) with $2\delta t\omega^{n+1}$ in the L^2 space, we have

$$\begin{aligned}(3\rho^{n+1}-4\rho^n+\rho^{n-1},\omega^{n+1})+2\delta t Q^{n+1}\int_\Omega \nabla\cdot(\mathbf{u}^*\rho^*)\omega^{n+1}d\boldsymbol{x}\\ +\ 2\delta t M_1\left\|\omega^{n+1}-\frac{1}{|\Omega|}\int_\Omega\omega^{n+1}d\boldsymbol{x}\right\|^2=0.\end{aligned}\tag{3.77}$$

Computing the L^2 inner product of (3.25) with $-(3\phi^{n+1}-4\phi^n+\phi^{n-1})$, we find

$$\begin{aligned}-(\omega^{n+1},3\rho^{n+1}-4\rho^n+\rho^{n-1})+\lambda_2\gamma(\nabla\rho^{n+1},\nabla(3\rho^{n+1}-4\rho^n+\rho^{n-1}))\\ +\ U^{n+1}\int_\Omega R^*(3\rho^{n+1}-4\rho^n+\rho^{n-1})d\boldsymbol{x}\\ +\ \frac{S_2}{\eta^2}(\rho^{n+1}-\rho^*,3\rho^{n+1}-4\rho^n+\rho^{n-1})=0.\end{aligned}\tag{3.78}$$

By multiplying (3.26) with $2U^{n+1}$ and using (3.69), we obtain

$$\begin{aligned}|U^{n+1}|^2-|U^n|^2+|2U^{n+1}-U^n|^2-|2U^n-U^{n-1}|^2+|U^{n+1}-2U^n+U^{n-1}|^2\\ =U^{n+1}\int_\Omega(H^*(3\phi^{n+1}-4\phi^n+\phi^{n-1})+R^*(3\rho^{n+1}-4\rho^n+\rho^{n-1}))d\boldsymbol{x}.\end{aligned}\tag{3.79}$$

By multiplying (3.28) with $2\delta t Q^{n+1}$ and using (3.69), we obtain

$$\begin{aligned}&\frac{1}{2}\Big(|Q^{n+1}|^2-|Q^n|^2+|2Q^{n+1}-Q^n|^2-|2Q^n-Q^{n-1}|^2+|Q^{n+1}-2Q^n+Q^{n-1}|^2\Big)\\ &=2\delta t Q^{n+1}\int_\Omega\nabla\cdot(\mathbf{u}^*\phi^*)\mu^{n+1}+2\delta t Q^{n+1}\int_\Omega(\phi^*\nabla\mu^*)\cdot\tilde{\mathbf{u}}^{n+1}d\boldsymbol{x}\\ &+2\delta t Q^{n+1}\int_\Omega\nabla\cdot(\mathbf{u}^*\rho^*)\omega^{n+1}d\boldsymbol{x}+2\delta t Q^{n+1}\int_\Omega\rho^*\nabla\omega^*\cdot\tilde{\mathbf{u}}^{n+1}d\boldsymbol{x}\\ &+2\delta t Q^{n+1}\int_\Omega(\mathbf{u}^*\cdot\nabla)\mathbf{u}^*\cdot\tilde{\mathbf{u}}^{n+1}d\boldsymbol{x}.\end{aligned}\tag{3.80}$$

Hence, by combining (3.74)–(3.80), we arrive at

$$\begin{aligned}&\frac{1}{2}(\|\mathbf{u}^{n+1}\|^2-\|\mathbf{u}^n\|^2+\|2\mathbf{u}^{n+1}-\mathbf{u}^n\|^2-\|2\mathbf{u}^n-\mathbf{u}^{n-1}\|^2)\\ &+\frac{2\delta t^2}{3}(\|\nabla p^{n+1}\|^2-\|\nabla p^n\|^2)\\ &+\frac{\lambda_1}{2}(\|\nabla\phi^{n+1}\|^2-\|\nabla\phi^n\|^2+\|\nabla(2\phi^{n+1}-\phi^n)\|^2-\|\nabla(2\phi^n-\phi^{n-1})\|^2)\\ &+\frac{\lambda_2\gamma}{2}(\|\nabla\rho^{n+1}\|^2-\|\nabla\rho^n\|^2+\|\nabla(2\rho^{n+1}-\rho^n)\|^2-\|\nabla(2\rho^n-\rho^{n-1})\|^2)\\ &+(|U^{n+1}|^2-|U^n|^2+|2U^{n+1}-U^n|^2-|2U^n-U^{n-1}|^2)\\ &+\frac{1}{2}(|Q^{n+1}|^2-|Q^n|^2+|2Q^{n+1}-Q^n|^2-|2Q^n-Q^{n-1}|^2)\\ &+\frac{S_1}{\epsilon^2}(\|\phi^{n+1}-\phi^n\|^2-\|\phi^n-\phi^{n-1}\|^2)+\frac{S_2}{\eta^2}(\|\rho^{n+1}-\rho^n\|^2-\|\rho^n-\rho^{n-1}\|^2)\\ &+\Big\{\frac{1}{2}\|\mathbf{u}^{n+1}-2\mathbf{u}^n+\mathbf{u}^{n-1}\|^2+\frac{3}{2}\|\mathbf{u}^{n+1}-\tilde{\mathbf{u}}^{n+1}\|^2\\ &\quad+\frac{\lambda_1}{2}\|\nabla(\phi^{n+1}-2\phi^n+\phi^{n-1})\|^2+\frac{\lambda_2\gamma}{2}\|\nabla(\rho^{n+1}-2\rho^n+\rho^{n-1})\|^2\end{aligned}$$

$$
\begin{aligned}
&+\frac{2S_1}{\epsilon^2}\|\phi^{n+1}-2\phi^n+\phi^{n-1}\|^2+\frac{2S_2}{\eta^2}\|\rho^{n+1}-2\rho^n+\rho^{n-1}\|^2\\
&+|U^{n+1}-2U^n+U^{n-1}|^2+\frac{1}{2}|Q^{n+1}-2Q^n+Q^{n-1}|^2\Big\}\\
&=-2\delta t\nu\|\nabla\tilde{\mathbf{u}}^{n+1}\|^2-2\delta tM_1\left\|\mu^{n+1}-\frac{1}{|\Omega|}\int_\Omega\mu^{n+1}d\boldsymbol{x}\right\|^2\\
&-2\delta tM_2\left\|\omega^{n+1}-\frac{1}{|\Omega|}\int_\Omega\omega^{n+1}d\boldsymbol{x}\right\|^2,
\end{aligned}
\tag{3.81}
$$

where we use the following identity:

$$
(3a-4b+c)(a-2b+c)=(a-b)^2-(b-c)^2+2(a-2b+c)^2. \tag{3.82}
$$

Finally, we obtain (3.64) from (3.81) after dropping the positive terms in { } and dividing both sides by 2. □

4. Numerical simulations

In this section, we implement numerical examples to verify the accuracy and energy stability of the proposed algorithm (3.22)–(3.30). Numerical simulations including accuracy/stability tests, spinodal decomposition in 2D and 3D, and collision of two droplets driven by the shear flow in 2D and 3D, are performed. In all numerical examples, we set the computational domain to be the rectangular shape. For directions with periodic boundary conditions, the Fourier-spectral method is used for discretization. For directions with boundary conditions specified in (3.32), the Legendre–Galerkin method is adopted for discretization. The inf–sup stable pair (P_N, P_{N-2}) is used for the velocity ($\tilde{\mathbf{u}}$ and $\mathbf{u}$) and pressure p, respectively, and P_N is used for the phase-field variables ϕ, ρ.

4.1. Accuracy and stability test

We first verify the accuracy and stability of the fully-decoupled scheme (3.22)–(3.30) using the scalar auxiliary variables (denoted by DSAV for short) by performing several convergence and stability tests. Assuming that the exact solution of the system (2.4)–(2.7) are given as follows:

$$
\begin{cases}
\phi(x,y,t)=\sin x\cos y\cos t,\ \rho(x,y,t)=(0.5+0.1\sin x\cos y)\cos t,\\
\mathbf{u}(x,y,t)=(u(x,y,t),v(x,y,t))=(\cos x\ \sin(2y),\sin x\ \sin^2 y)\cos t,\\
p(x,y,t)=\sin x\sin y\sin t.
\end{cases}
\tag{4.1}
$$

We apply some suitable force fields so that the functions given in (4.1) can satisfy the system. The 2D computational domain is set to be $\Omega=[0,2\pi]^2$, and the order parameters read as

$$
\begin{aligned}
&M_1=M_2=0.01,\lambda_1=\lambda_2=0.01,\epsilon=0.1,\eta=0.1,\\
&\theta_1=0.1,\theta_2=0.1,\zeta=1\text{e}{-5},\nu=1,S_1=S_2=0.05.
\end{aligned}
\tag{4.2}
$$

We assume that the x-direction meets the periodic boundary conditions and use 129 Fourier modes for discretization. The y-direction satisfies the boundary conditions given in (2.12) and is discretized by using the Legendre–Galerkin method where the Legendre polynomials with degrees up to 128 are used. Such a fine mesh can make the spatial discretization error negligible compared with the time discretization error. In Fig. 4.1(a), we plot the L^2 errors of all unknown variables between the numerical solution and the exact solution at $t=0.5$ by varying the time step from $\delta t=0.01$ to $\delta t=\frac{0.01}{2^4}$ with a factor of 1/2. We observe that the DSAV exhibits perfect second-order accuracy for ϕ, ρ and $\mathbf{u}=(u,v)$, first-order accuracy for p, as expected.

By performing more mesh refinement examples in time, we further test the convergence speed of the developed solution DSAV. The calculation domain, boundary conditions, spatial discretization, and the number of grid points are the same as the previous example. The initial conditions are set as follows (shown in the first subfigure of Fig. 4.4),

$$
\begin{cases}
\phi^0(x,y)=1+\sum_{i=1}^{2}\tanh\left(\frac{r_i-\sqrt{(x-x_i)^2+(y-y_i)^2}}{1.5\epsilon}\right),\\
\mathbf{u}^0(x,y)=\mathbf{0},\ p^0(x,y)=0,
\end{cases}
\tag{4.3}
$$

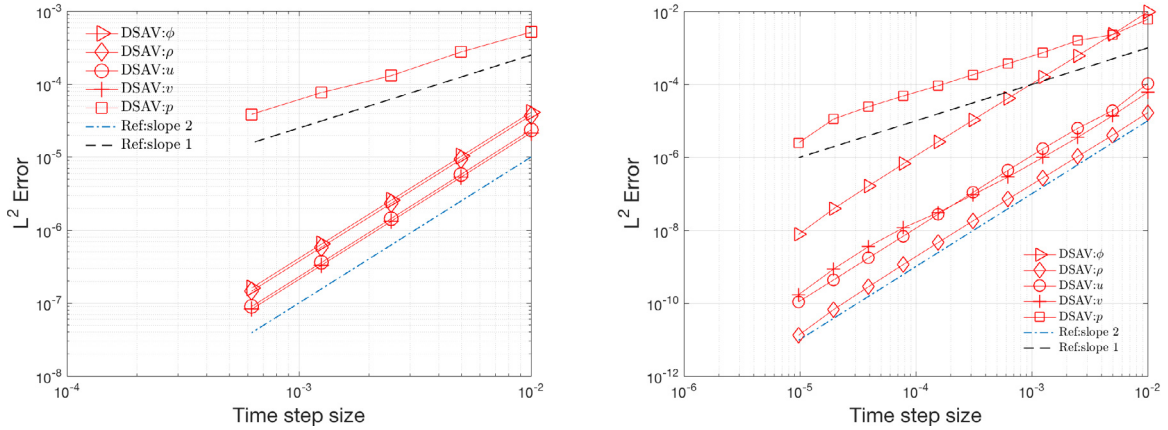

(a) Presume exact solution. (b) Mesh refinement in time.

Fig. 4.1. Accuracy tests where (a) the presumed exact solutions are given in (4.1), and (b) mesh refinement in time with the initial solution given in (4.3). In both subfigures, the L^2 numerical errors of ϕ, ρ, $\mathbf{u} = (u, v)$, p, are computed by using the scheme DSAV with different time steps.

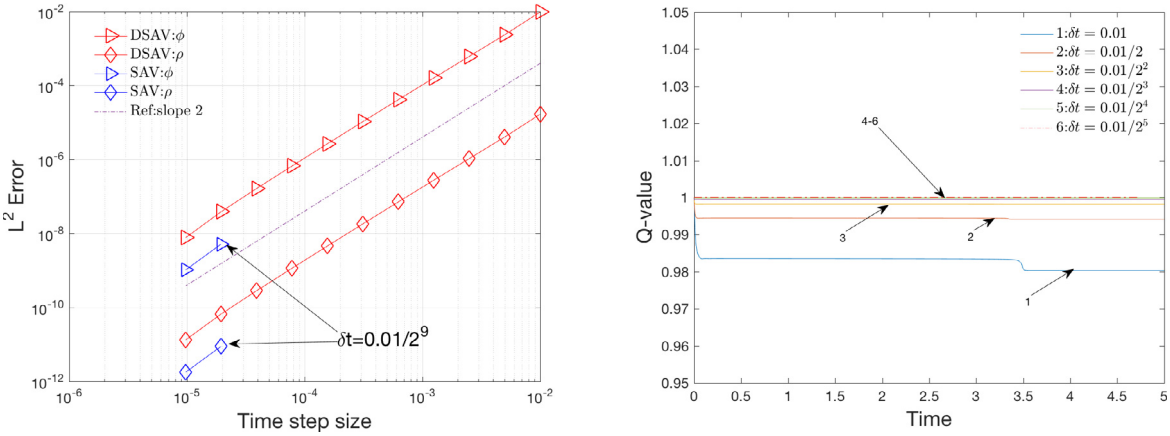

(a) DSAV and SAV. (b) Evolution of Q over time.

Fig. 4.2. (a) The comparison of accuracy computed by the scheme DSAV and SAV with various time steps and the given initial conditions (4.3), where the L^2 numerical errors of ϕ and ρ are plotted, and (b) the time evolution of the nonlocal variable Q.

where $r_1 = 1.4$, $r_2 = 0.7$, $x_1 = \pi - 0.8$, $x_2 = \pi + 1.7$, $y_1 = y_2 = \pi$. We set the parameters as

$$\begin{aligned} &M_1 = M_2 = 20, \lambda_1 = \lambda_2 = 0.01, \epsilon = 0.05, \eta = 0.005, \\ &\theta_1 = 0.02, \theta_2 = 2, \zeta = 1\text{e}{-5}, \nu = 1, S_1 = S_2 = 0.05. \end{aligned} \tag{4.4}$$

Since the exact solution is unknown, the numerical solution obtained by the scheme DSAV using a very small time step $\delta t = 1\text{e}{-9}$ will be treated as the exact solution to calculate the approximate errors. Then, we choose $t = 0.5$ and plot the L^2 errors of all variables obtained by changing the time step from 0.01 to $t = 0.01/2^{10}$ with a factor of $1/2$. The convergence rate is shown in Fig. 4.1(b), where we find that the scheme DSAV always exhibits almost perfect second-order accuracy for ϕ, ρ, $\mathbf{u} = (u, v)$, and first-order accuracy for p.

Furthermore, we examine the effect of the added stabilizers S_1, S_2 on stability and accuracy. For simplicity, we use SAV to represent the scheme in which $S_1 = S_2 = 0$. In Fig. 4.2(a), we compare the accuracy of DSAV and SAV by plotting the L^2 numerical errors of ϕ and ρ at $t = 0.5$ obtained by using different time steps. When the time step size is large ($\delta t > \frac{0.01}{2^9}$), SAV overflows and the accuracy is lost. When the time step size is small ($\delta t \leq \frac{0.01}{2^9}$), it shows the second-order accuracy for ϕ and ρ. But DSAV always shows good second-order accuracy for all tested

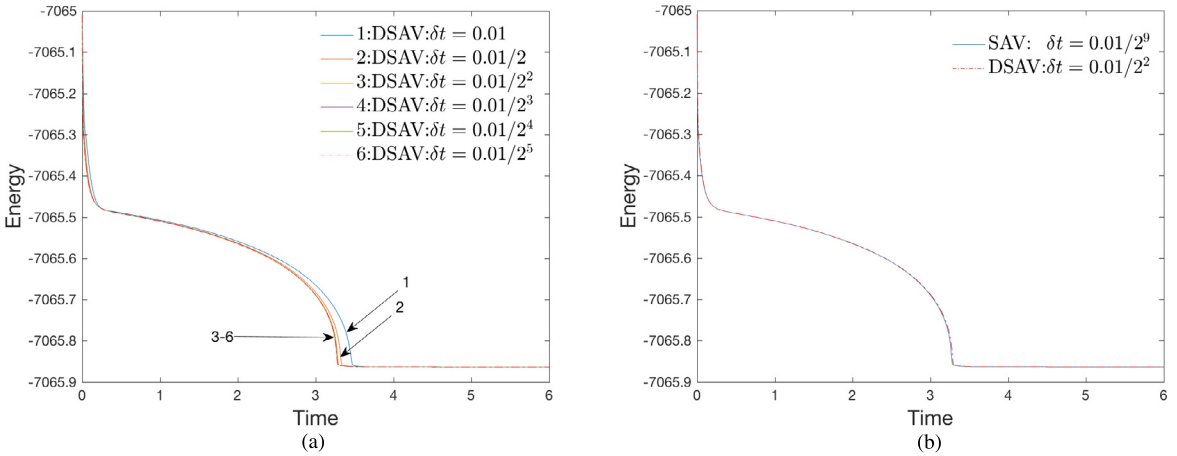

Fig. 4.3. (a) The evolution of the total free energy (3.65) over time computed by using DSAV and different time steps. (b) The evolution of the total free energy (3.65) over time computed by using DSAV with $\delta t = 0.01/2^2$ and SAV with $\delta t = 0.01/2^9$.

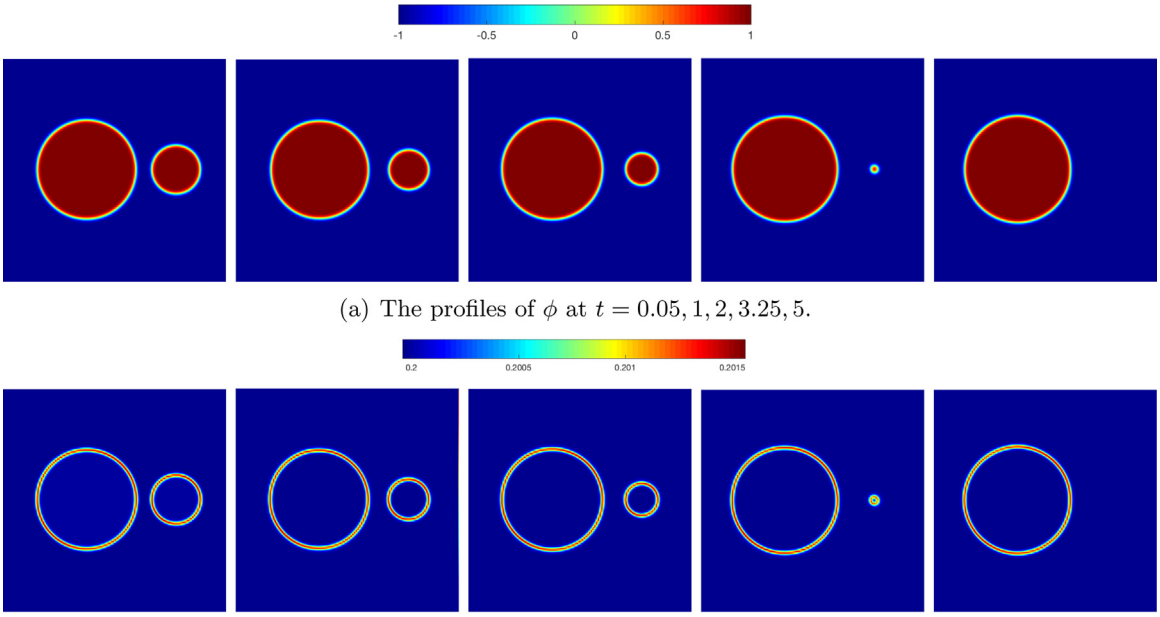

(a) The profiles of ϕ at $t = 0.05, 1, 2, 3.25, 5$.

(b) The profiles of ρ at $t = 0.05, 1, 2, 3.25, 5$.

Fig. 4.4. Snapshots of the profiles of ϕ and ρ at various times with the initial conditions given in (4.3) computed by the scheme DSAV with $\delta t = 0.01/2^2$.

time steps. If we compare the size of the error when $\delta t \leq \frac{0.01}{2^9}$, we find that the error obtained by SAV is smaller than that obtained by DSAV. This is because the two extra stabilizers used in DSAV also increase some splitting errors. In Fig. 4.2(b), we plot the evolution of the value of Q over time computed using different time steps is plotted. We find that the value of Q has always been very close to 1. When the step size is small, it is almost equal to 1.

Next, we use different time steps to perform energy stability tests. In Fig. 4.3(a), we plot six energy evolution curves computed by using DSAV with time steps from $\delta t = 0.01$ to $0.01/2^5$ with factor of $1/2$. All obtained curves show very good monotonic decay. When the time step is very large, such as $\delta t = 0.01$, the deviation between the energy curve and other curves obtained with smaller steps is relatively large due to large computational errors.

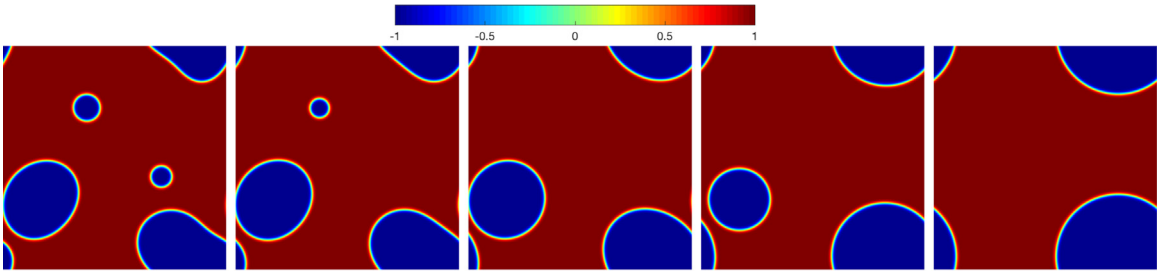

(a) Snapshots of ϕ at $t = 1.5, 2, 5, 15, 35$.

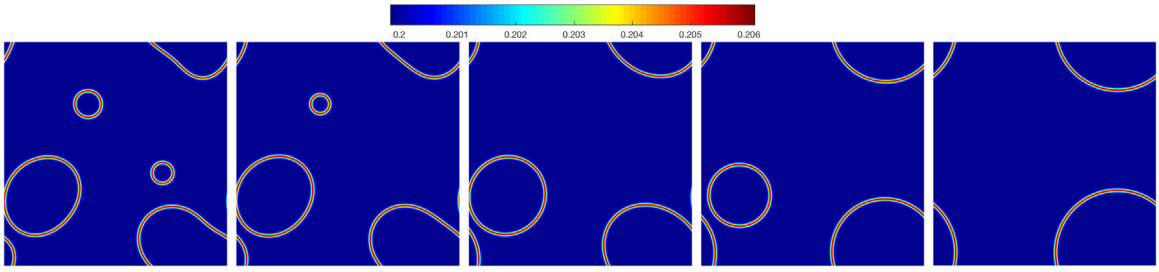

(b) Snapshots of ρ at $t = 1.5, 2, 5, 15, 35$.

Fig. 4.5. 2D spinodal decomposition example, where snapshots of the profiles of ϕ and ρ are plotted at $t = 1.5, 2, 5, 15, 35$.

When the step size is less than $0.01/2^2$, all the energy curves are overlapped together, which represents that the computational results reach the expected degree. In Fig. 4.3(b), we plot two energy evolution curves, one of which is calculated by SAV using a very small time step $\delta t = 0.01/2^9$. All calculations using SAV with large step sizes will eventually overflow, therefore the energy evolution curves cannot be plotted, and the time step size $\delta t = 0.01/2^9$ used in Fig. 4.3(b) is the maximum step size that SAV allows. At the same time, we also plot the energy curve computed by DSAV with $\delta t = 0.01/2^2$. It can be seen that the two curves are completely coincident, so we can say that the stabilized algorithm DSAV can use very large time steps. For this example, the step size used by DSAV can be increased to 128 times than that of SAV.

Finally, we implement DSAV to the equilibrium state by using the time step size $\delta t = \frac{0.1}{2^2}$. Snapshots of the profile ϕ and ρ at various times are shown in Fig. 4.4, where we find that the small circle is absorbed into the large circle gradually under the effect of coarsening. Meanwhile, we can see that concentration is high around the fluid interfaces due to the coupling potential associated with θ_1 and θ_2.

4.2. Spinodal decomposition in 2D and 3D

In this example, we set the initial conditions of the local density variable ρ to a homogeneous medium with small disturbances to study the phase separation (spinodal decomposition) process over time.

We first perform a 2D simulation with the computed domain $[0, 2\pi]^2$. The initial conditions are set as follows,

$$\mathbf{u}^0(\boldsymbol{x}) = 0,\ p^0(\boldsymbol{x}) = 0,\ \phi(\boldsymbol{x}) = 0.5 + 0.001\text{rand}(\boldsymbol{x}),\ \rho(\boldsymbol{x}) = 0.2, \tag{4.5}$$

where the rand($\boldsymbol{x}$) is the random number in $[-1, 1]$ that follows the normal distribution. We assume periodic boundary conditions and discretize the space by using 257 Fourier modes for each direction. We set the model parameters as

$$\begin{aligned} &M_1 = M_2 = 20, \lambda_1 = \lambda_2 = 0.01, \epsilon = 0.05, \eta = 0.01, \theta_1 = 0.02, \\ &\theta_2 = 1, \zeta = 1\text{e}{-5}, \nu = 1, S_1 = S_2 = 0.05, B = 1e5, \delta t = 0.001. \end{aligned} \tag{4.6}$$

In Fig. 4.5, we plot snapshots of ϕ and ρ at different times. We observe that the final equilibrium solution of the fluid interface exhibits a circular state, and the concentration variable ρ presents a relatively high value at the fluid interface.

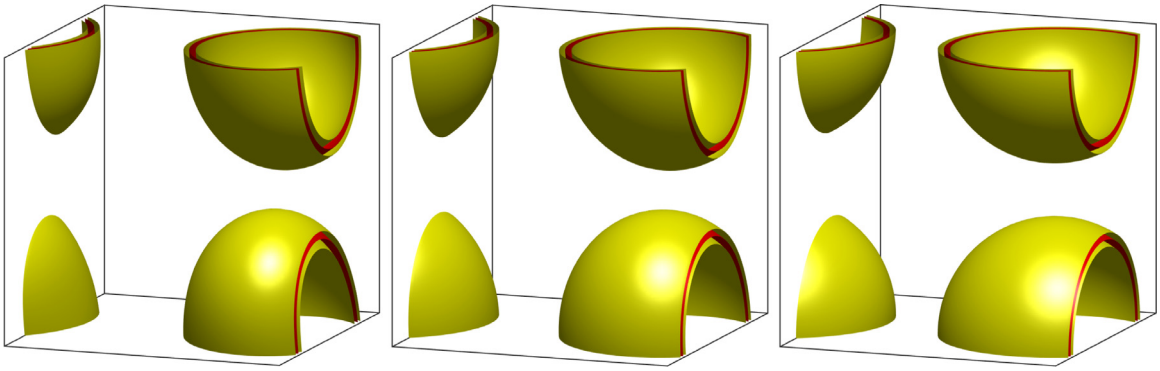

Fig. 4.6. 3D spinodal decomposition example, where snapshots of the isosurfaces of $\{\phi = 0\}$ (in the color red) and $\{\rho = 0.21\}$ (in the color yellow, 0.21 is near the maximum value of ρ) are plotted at $t = 0.8$, 1, and 5. (For interpretation of the references to color in this figure legend, the reader is referred to the web version of this article.)

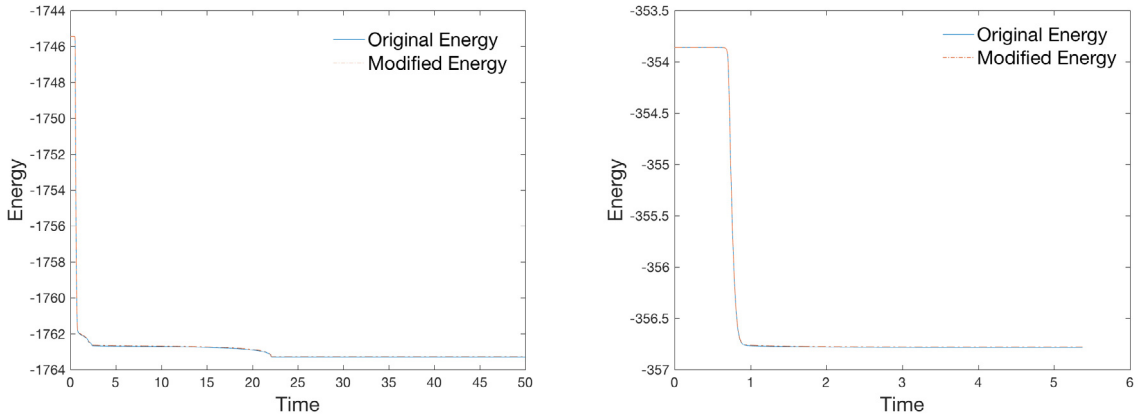

(a) Energy evolution for 2D spinodal decomposition. (b) Energy evolution for 3D spinodal decomposition.

Fig. 4.7. Comparison of the total free energy in the original form (2.2) and modified form (3.65) computed by using the scheme DSAV for the spinodal decomposition examples in 2D and 3D.

We use the same initial conditions given in (4.5) to perform a 3D simulation. The computational domain is $[0, 2\pi]^3$ and order parameters are the same as the 2D simulation. In Fig. 4.6, snapshots of the isosurfaces of $\{\phi = 0\}$ and $\{\rho = 0.21\}$ (near the maximum value of ρ) are plotted using different colors, red and yellow, respectively. We find that the dynamics of phase separation are similar to the 2D simulation, and the final steady-state appears to be a spherical phase. In Fig. 4.7, we plot the evolutions of the total free energy in the original form (2.2) and modified form (3.65) over time, all curves show a monotonic decaying structure.

Finally, in Fig. 4.8, we exhibit the equilibrium solutions of 2D and 3D spinodal decomposition examples obtained using the two models, the conserved Allen–Cahn model developed in this paper and the classical Cahn–Hilliard model [4,7,8] where the nonlinear potential $\tilde{G}(\rho)$ is used. All other computational settings are the same. We can see that although the models are different, the equilibrium phase obtained is the same.

4.3. Collision of two droplets driven by shear flow in 2D and 3D

In this example, we consider the motion of two closely deposited droplets under the action of an applied shear flow. When the droplets are about to collide, there will be some differences between the surfactant and non-surfactant cases.

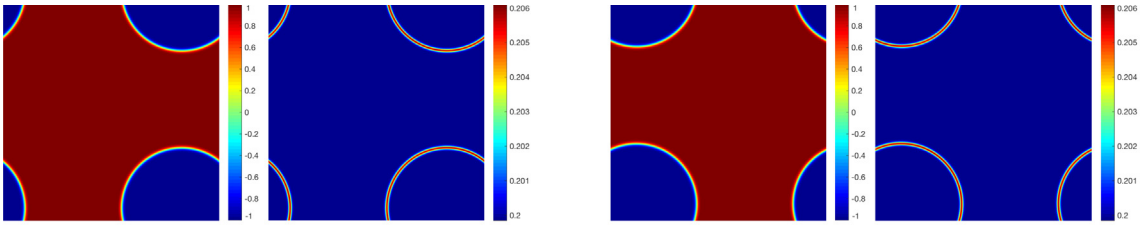

(a) Snapshots of the equilibrium solution of the 2D spinodal decomposition example computed using the conserved Allen-Cahn model (ϕ and ρ are the two figures on the left), and the classical Cahn-Hilliard model (ϕ and ρ are the two figures on the right).

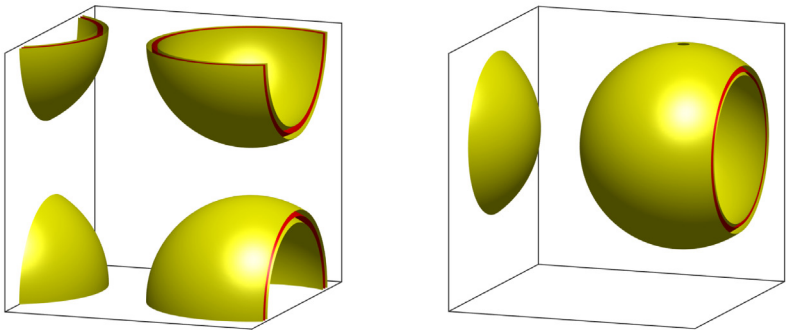

(b) Snapshots of the equilibrium solution of the isosurfaces of $\{\phi = 0\}$ (in the color red) and $\{\rho = 0.21\}$ (in the color yellow) in 3D for the conserved Allen-Cahn system (left), and the classical Cahn-Hilliard system (right).

Fig. 4.8. Comparison of 2D and 3D equilibrium solution using the conserved Allen–Cahn system and the classical Cahn–Hilliard system using the same model parameters and initial conditions.

We first perform 2D simulations and set the computed domain as $\Omega = [0, 2]^2$. We set the initial conditions as follows.

$$\begin{aligned} &\phi^0 = \sum_{i=1}^{2} \tanh\left(\frac{\sqrt{r_i - (x - x_i)^2 - (y - y_i)^2}}{\epsilon}\right) + 1,\ \rho^0 = 0.2, \\ &\mathbf{u}^0 = (-0.7(y - 1), 0),\ p^0 = 0, \end{aligned} \tag{4.7}$$

where $(x_1, y_1, r_1) = (0.8, 1.266, 0.28)$ and $(x_2, y_2, r_2) = (1.2, 0.734, 0.28)$. The periodic boundary conditions are assumed along the x-direction. The boundary conditions for the y-direction are set as follows,

$$u|_{(y=0)} = 0.7, u|_{(y=2)} = -0.7, v|_{(y=0,y=2)} = 0, \phi_y|_{(y=0,y=2)} = \rho_y|_{(y=0,y=2)} = 0. \tag{4.8}$$

We use the Fourier-spectral method to discretize the x-direction and 257 Fourier modes are used. The spatial discretization for y-direction is based on the Legendre–Galerkin method and Legendre polynomials with degrees up to 256 are used. We set the model parameters as

$$\begin{aligned} &M_1 = M_2 = 1, \lambda_1 = \lambda_2 = 0.01, \epsilon = 0.02, \eta = 0.005, \\ &\zeta = 1\text{e}{-5}, \nu = 1, S_1 = S_2 = 0.5, B = 1e5, \delta t = 1\text{e}{-3}. \end{aligned} \tag{4.9}$$

We first neglect the surfactant effects by setting the coupling parameter $\theta_1 = \theta_2 = 0$. In Fig. 4.9, snapshots of the phase-field variable ϕ at different times are plotted. We observe that, under the action of the shear flow, the two droplets start to move in the opposite direction. As time goes by, around $t = 0.8$, because the distance between the two droplets is very close, they collide and then merge into a larger droplet. For comparison, we restore the surfactant effects by setting the coupling parameter $\theta_1 = 0.025, \theta_2 = 6$ and all other model parameters are the same as the no-surfactant simulation. In Fig. 4.10(a) and (b), snapshots of ϕ and ρ at different times are shown, respectively. We find that even when the two droplets are very close, they will not merge but slip away from each

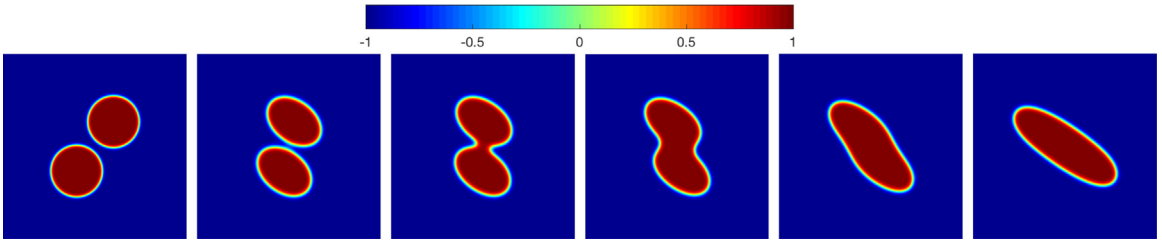

Fig. 4.9. Two 2D droplets driven by the shear flow without surfactant effects ($\theta_1 = \theta_2 = 0$), where the snapshots at $t = 0$, 0.8, 1, 1.35, 2, and 3 are taken for the phase-field variable ϕ.

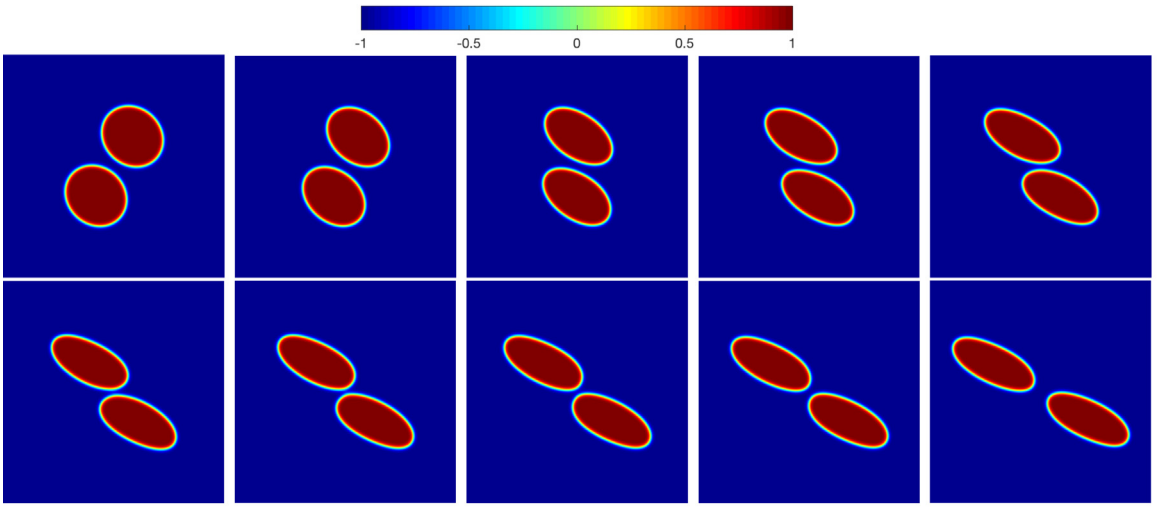

(a) Snapshots of ϕ at $t = 0.2, 0.5, 1, 1.5, 2, 2.25, 2.5, 2.75, 3, 3.5$.

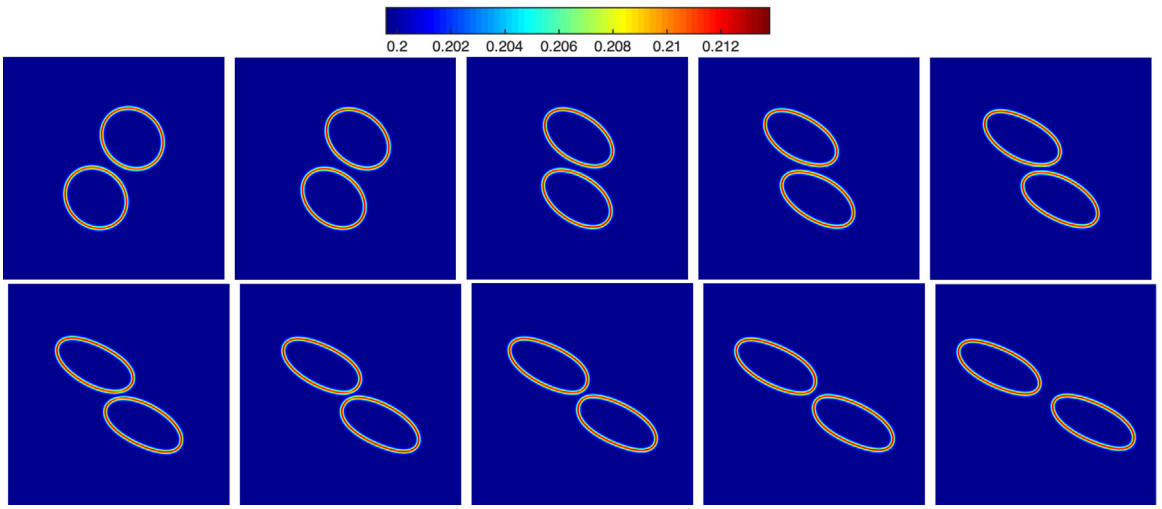

(b) Snapshots of ρ at $t = 0.2, 0.5, 1, 1.5, 2, 2.25, 2.5, 2.75, 3, 3.5$.

Fig. 4.10. Two 2D droplets driven by the shear flow with surfactant effects ($\theta_1 = 0.025$, $\theta_2 = 6$). Snapshots of the phase-field variable ϕ are taken at $t = 0.2, 0.5, 1, 1.5, 2, 2.25, 2.5, 2.75, 3, 3.5$.

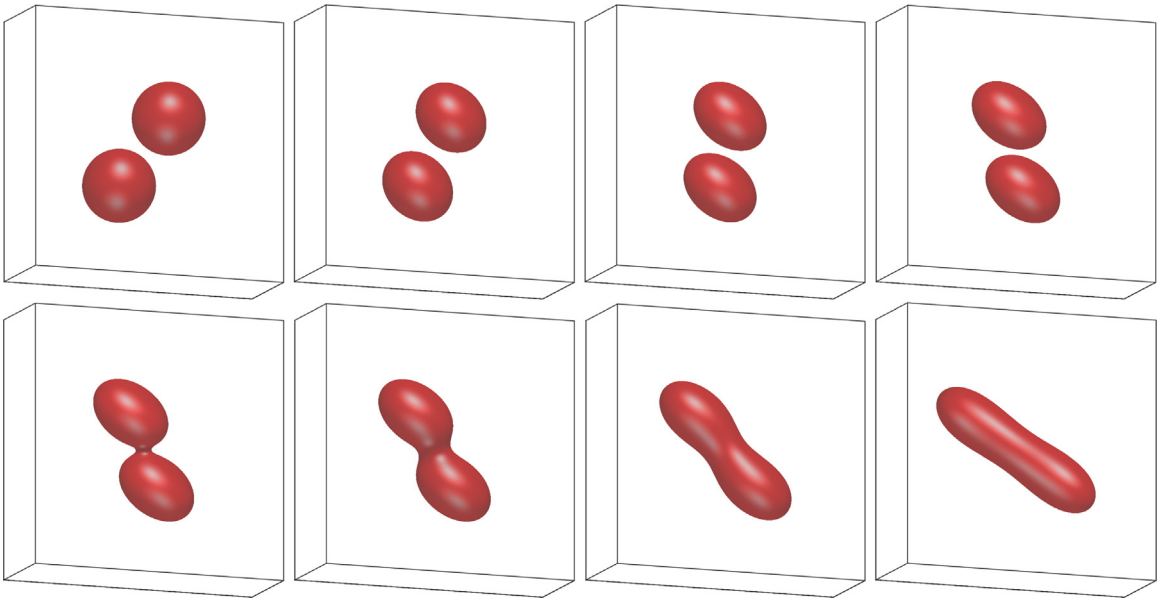

Fig. 4.11. Two 3D droplets driven by the shear flow without surfactant effects ($\theta_1 = \theta_2 = 0$). Snapshots of the isosurfaces of $\{\phi = 0\}$ are taken at $t = 0$, 0.5, 1, 1.5, 1.75, 2, 2.5, and 3.5.

other, which means that the role of the surfactant can overcome the coarsening effect. In [44–46], similar behaviors have also been experimentally observed, and similar 2D simulations were also reported in [3] by using an alternative phase-field surfactant model.

We continue to perform 3D simulations. The computed domain is set as $\Omega = [0, 2] \times [0, 0.7] \times [0, 2]$, and the initial conditions are set as follows.

$$\begin{aligned} &\phi^0 = \sum_{i=1}^{2} \tanh\left(\frac{\sqrt{r_i - (x - x_i)^2 - (y - y_i)^2 + (z - z_i)^2}}{\epsilon}\right) + 1, \rho^0 = 0.2, \\ &\mathbf{u}^0 = (0.7(y - 1), 0, 0), p^0 = 0, \end{aligned} \tag{4.10}$$

where $(x_1, y_1, z_1, r_1) = (0.8, 0.35, 1.272, 0.28)$ and $(x_2, y_2, z_2 r_2) = (1.2, 0.35, 0.728, 0.28)$. The periodic boundary conditions are assumed for the x and y directions which are then discretized by using Fourier-Spectral method with 129 Fourier modes for each direction. The boundary conditions for the variables $\mathbf{u} = (u, v, w)$, ϕ, ρ along the z-direction are set as follows,

$$u|_{z=0} = 0.7, u|_{z=2} = -0.7, (v, w, \phi_y, \rho_y)|_{z=0,2} = 0. \tag{4.11}$$

The spatial discretization for the z-direction is based on the Legendre–Galerkin method and Legendre polynomials with degrees up to 256 are used for discretization. The order parameters read as

$$\begin{aligned} &M_1 = M_2 = 1, \lambda_1 = \lambda_2 = 0.01, \epsilon = 0.015, \eta = 0.005, \\ &\zeta = 1\text{e}{-5}, \nu = 1, S_1 = S_2 = 0.5, B = 1e5, \delta t = 1\text{e}{-3}. \end{aligned} \tag{4.12}$$

Similar to the 2D case, the 3D simulations without surfactant effects ($\theta_1 = \theta_2 = 0$) are first simulated and snapshots of the interface $\{\phi = 0\}$ are plotted in Fig. 4.11. When the two droplets move to a very close distance, the coarsening effect allows them to merge into a larger droplet. But after imposing the surfactant effects with $\theta_1 = 0.02, \theta_2 = 2$, from the plots of isosurfaces of $\{\phi = 0\}$ and $\{\rho = 0.21\}$ shown in Fig. 4.12(a) and (b), respectively, we observe that the two droplets slide and finally depart from each other.

5. Concluding remarks

We consider two things in this article. First, we replace the fourth-order Cahn–Hilliard model with the conserved Allen–Cahn equation and rebuild simpler hydrodynamics coupled binary fluid surfactant model. Second, in order

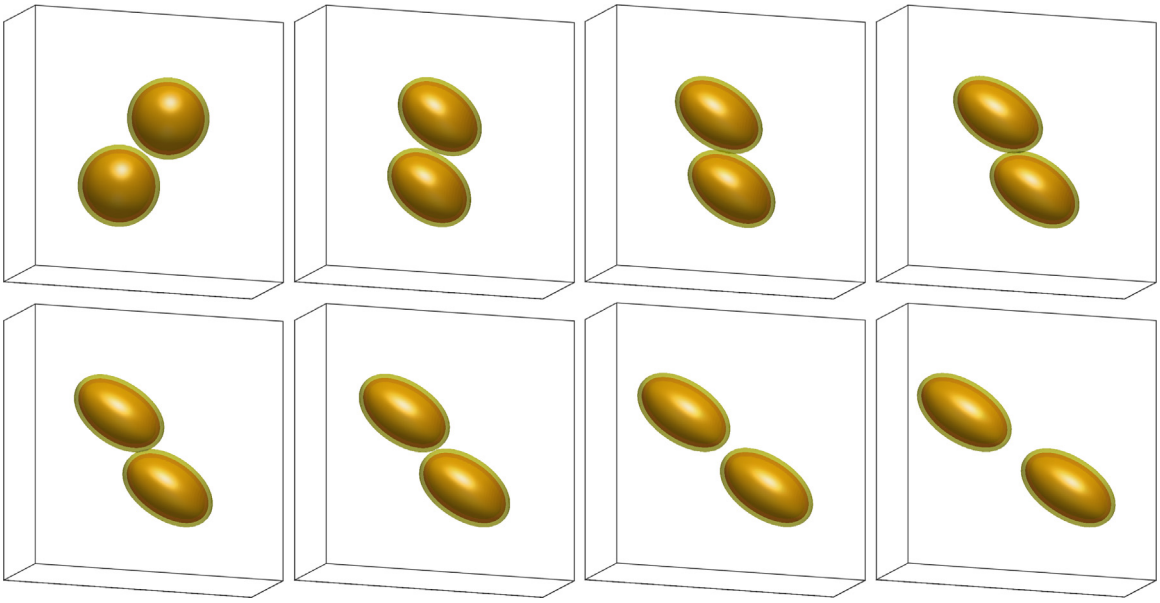

Fig. 4.12. Two 3D droplets driven by the shear flow with surfactant effects ($\theta_1 = 0.02, \theta_2 = 2$). Snapshots of the isosurfaces of $\{\phi = 0\}$ (in the color red) and $\{\rho = 0.21\}$ (in the color yellow) are taken at $t = 0.1$, 1, 1.5, 2, 2.25, 2.5, 3, and 3.5. (For interpretation of the references to color in this figure legend, the reader is referred to the web version of this article.)

to solve this model, we propose a novel fully-decoupled scheme with second-order accuracy in time. At each time step, we only need to solve several linear elliptic equations with constant coefficients to obtain second-order accurate numerical solutions. Moreover, we give a detailed practical implementation method and strictly prove the unconditional energy stability of the scheme. Finally, through the implementation of a large number of numerical examples, the effectiveness of the model and numerical scheme are proved. *As far as the author knows, this is the first fully-decoupled and second-order time-accurate scheme of the flow-coupled phase-field type model.* With great versatility and flexibility, the novel decoupling method designed in this paper can be combined with any linear scheme of the flow-coupled phase-field model (e.g. the linear stabilization, IEQ, or SAV, etc.) to form a fully-decoupled numerical scheme.

Declaration of competing interest

The authors declare that they have no known competing financial interests or personal relationships that could have appeared to influence the work reported in this paper.

Acknowledgment

X. Yang was partially supported by National Science Foundation, United States of America with grant numbers DMS-1720212, 1818783, and 2012490.

References

[1] M. Laradji, H. Guo, M. Grant, M.J. Zuckermann, The effect of surfactants on the dynamics of phase separation, J. Phys.: Condens. Matter 4 (32) (1992) 6715.
[2] M. Laradji, O.G. Mouristen, S. Toxvaerd, M.J. Zuckermann, Molecular dynamics simulatiens af phase separation in the presence ef surfactants, Phys. Rev. E. 50 (1994) 1722–1727.
[3] H. Liu, Y. Zhang, Phase-field modeling droplet dynamics with soluble surfactants, J. Comput. Phys. 229 (2010) 9166–9187.
[4] J. Zhang, C. Chen, J. Wang, X. Yang, Efficient, second order accurate, and unconditionally energy stable numerical scheme for a new hydrodynamics coupled binary phase-field surfactant system, Comput. Phys. Comm. 251 (2020) 107122.
[5] T. Teramoto, F. Yonezawa, Droplet growth dynamics in a water-oil-surfactant system, J. Colloid Inter. Sci. 235 (2001) 329–333.
[6] S. Komura, H. Kodama, Two-order-parameter model for an oil-water-surfactant system, Phys. Rev. E. 55 (1997) 1722–1727.

[7] R.G.M. van der Sman, M.B.J. Meinders, Analysis of improved lattice Boltzmann phase field method for soluble surfactants, Comput. Phys. Comm. 199 (2016) 12–21.
[8] R. van der Sman, S. van der Graaf, Diffuse interface model of surfactant adsorption onto flat and droplet interfaces, Rheol. Acta 46 (2006) 3–11.
[9] G. Gompper, M. Schick, in: C. Domb, J. Lebowitz (Eds.), Self-Assembling Amphiphilic Systems, in Phase Trasitions and Critical Phenomena, Vol. 16, Academic Press, London, 1994.
[10] C.H. Teng, I.L. Chern, M.C. Lai, Simulating binary fluid-surfactant dynamics by a phase field model, Dis. Conti. Dyn, Syst.-B 17 (2010) 1289–1307.
[11] I. Fonseca, M. Morini, V. Slastikov, Surfactants in foam stability: A phase-field approach, Arch. Ration. Mech. Anal. 183 (2007) 411–456.
[12] J. Kim, Numerical simulations of phase separation dynamics in a water-oil-surfactant system, J. Colloid Interface Sci. 303 (2006) 272–279.
[13] X. Yang, Numerical approximations for the Cahn–Hilliard phase field model of the binary fluid-surfactant system, J. Sci. Comput. 74 (2017) 1533–1553.
[14] X. Yang, L. Ju, Linear and unconditionally energy stable schemes for the binary fluid-surfactant phase field model, Comput. Methods Appl. Mech. Engrg. 318 (2017) 1005–1029.
[15] R. Nochetto, J.-H. Pyo, The Gauge–Uzawa finite element method part I: the Navier-Stokes equations, SIAM J. Numer. Anal. 43 (2005) 1043–1068.
[16] J.L. Guermond, P. Minev, J. Shen, An overview of projection methods for incompressible flows, Comput. Methods Appl. Mech. Engrg. 195 (2006) 6011–6045.
[17] J.L. Guermond, L. Quartapelle, A projection FEM for variable density incompressible flows, J. Comput. Phys. 165 (1) (2000) 167–188.
[18] R. Rannacher, On Chorin's projection method for the incompressible Navier-Stokes equations, in: The Navier-Stokes Equations II. Theory and Numerical Methods, in: Lecture Notes in Mathematics, vol. 1530, 1991, pp. 167–183.
[19] J.L. Guermond, J. Shen, On the error estimates of rotational pressure-correction projection methods, Math. Comp. 73 (2004) 1719–1737.
[20] J.L. Guermond, A. Salgado, A splitting method for incompressible flows with variable density based on a pressure Poisson equation, J. Comput. Phys. 228 (1) (2009) 2834–2846.
[21] C. Liu, J. Shen, X. Yang, Decoupled energy stable schemes for a phase-field model of two-phase incompressible flows with variable density, J. Sci. Comput. 62 (2015) 601–622.
[22] J. Shen, X. Yang, A phase-field model and its numerical approximation for two-phase incompressible flows with different densities and viscositites, SIAM J. Sci. Comput. 32 (2010) 1159–1179.
[23] J. Shen, X. Yang, Numerical approximations of Allen–Cahn and Cahn–Hilliard equations, Disc. Conti. Dyn. Sys.-A 28 (2010) 1669–1691.
[24] H. Yu, X. Yang, Numerical approximations for a phase-field moving contact line model with variable densities and viscosities, J. Comput. Phys. 334 (2017) 665–686.
[25] J. Shen, X. Yang, Decoupled, energy stable schemes for phase-field models of two-phase incompressible flows, SIAM J. Num. Anal. 53 (1) (2015) 279–296.
[26] J. Shen, C. Wang, S. Wang, X. Wang, Second-order convex splitting schemes for gradient flows with Ehrlich–Schwoebel type energy: application to thin film epitaxy, SIAM J. Numer. Anal. 50 (1) (2012) 105–125.
[27] D.J. Eyre, Unconditionally gradient stable time marching the Cahn–Hilliard equation, in: Computational and Mathematical Models of Microstructural Evolution (San Francisco, CA, 1998), in: Mater. Res. Soc. Sympos. Proc., vol. 529, MRS, Warrendale, PA, 1998, pp. 39–46.
[28] S.M. Wise, C. Wang, J.S. Lowengrub, An energy-stable and convergent finite-difference scheme for the phase field crystal equation, SIAM J. Numer. Anal. 47 (3) (2009) 2269–2288.
[29] Z. Hu, S.M. Wise, C. Wang, J.S. Lowengrub, Stable and efficient finite difference nonlinear-multigrid schemes for the phase field crystal equation, J. Comput. Phys. 228 (2009) 5323–5339.
[30] D. Han, X. Wang, A second order in time, uniquely solvable, unconditionally stable numerical scheme for Cahn–Hilliard–Navier–Stokes equation, J. Comput. Phys. 290 (2015) 139–156.
[31] X. Yang, H. Yu, Efficient second order unconditionally stable schemes for a phase field moving contact line model using an invariant energy quadratization approach, SIAM J. Sci. Comput. 40 (2018) B889–B914.
[32] X. Yang, J. Zhao, Q. Wang, J. Shen, Numerical Approximations for a three components Cahn–Hilliard phase-field Model based on the Invariant Energy Quadratization method, M3AS: Math. Models Methods Appl. Sci. 27 (2017) 1993–2030.
[33] X. Yang, Linear, first and second order and unconditionally energy stable numerical schemes for the phase field model of homopolymer blends, J. Comput. Phys. 327 (2016) 294–316.
[34] C. Chen, X. Yang, Efficient numerical scheme for a dendritic solidification phase field model with melt convection, J. Comput. Phys. 388 (2019) 41–62.
[35] J. Shen, J. Xue, J. Yang, The scalar auxiliary variable (SAV) approach for gradient flows, J. Comput. Phys. 353 (2018) 407–416.
[36] C. Chen, X. Yang, Fast, provably unconditionally energy stable, and second-order accurate algorithms for the anisotropic Cahn–Hilliard model, Comput. Meth. Appl. Mech. Eng. 351 (2019) 35–59.
[37] Z. Yang, S. Dong, An unconditionally energy-stable scheme based on an implicit auxiliary energy variable for incompressible two-phase flows with different densities involving only precomputable coefficient matrices, J. Comput. Phys. 393 (2018) 229–257.
[38] Q. Du, R.A. Nicolaides, Numerical analysis of a continuum model of phase transition, SIAM J. Numer. Anal. 28 (1991) 1310–1322.
[39] H. Gomez, der Zee Van, G. Kristoffer, Computational phase-field modeling, in: Encyclopedia of Computational Mechanics, second ed., John Wiley & Sons, Ltd, ISBN: 978-1-119-00379-3, 2017.

[40] H. Gomez, V.M. Calo, Y. Bazilevs, T.J.R. Hughes, Isogeometric analystis of the Cahn–Hilliard phase-field model, Comput. Methods Appl. Mech. Engrg. 197 (2008) 4333–4352.
[41] I. Romero, Thermodynamically consistent time stepping algorithms for nonlinear thermomechanical systems, Internat. J. Numer. Methods Engrg. 79 (2009) 706–732.
[42] S. Minjeaud, An unconditionally stable uncoupled scheme for a triphasic Cahn–Hilliard/Navier–Stokes model, Numer. Methods Partial Differential Equations 29 (2013) 584–618.
[43] W. E, J.-G. Liu, Projection method I: Convergence and numerical boundary layers, SIAM J. Numer. Anal. 32 (4) (1995) 1017–1057.
[44] Y.T. Hu, D.J. Pine, L.G. Leal, Drop deformation, breakup, and coalescence with compatibilizer, Phys. Fluids. 3 (2000) 484–489.
[45] S. Lyu, T.D. Jones, F.S. Bates, C.W. Macosko, Role of block copolymers on suppression of droplet coalescence, Macromolecules 35 (2002) 7845–7855..
[46] Y. Yoon, A. Hsu, L. Leal, Experimental investigation of the effects of copolymer surfactants on flow-induced coalescence of drops, Phys. Fluids 19 (2007) 023102.